

## Research Article

# Spatiotemporal Evolution Characteristics of Fluid Flow through Large-Scale 3D Rock Mass Containing Filling Joints: An Experimental and Numerical Study

Qian Yin <sup>1,2</sup>, Hongwen Jing,<sup>1</sup> Tantan Zhu,<sup>3</sup> Lizhou Wu <sup>2</sup>, Haijian Su <sup>1</sup> and Liyuan Yu <sup>1</sup>

<sup>1</sup>State Key Laboratory for Geomechanics and Deep Underground Engineering, China University of Mining and Technology, Xuzhou 221116, China

<sup>2</sup>State Key Laboratory of Geohazard Prevention and Geoenvironment Protection, Chengdu University of Technology, Chengdu 610059, China

<sup>3</sup>School of Highway, Changan University, Xian 710064, China

Correspondence should be addressed to Lizhou Wu; [wulizhou07@cdut.cn](mailto:wulizhou07@cdut.cn)

Received 9 September 2020; Accepted 15 December 2020; Published 4 January 2021

Academic Editor: Feng Xiong

Copyright © 2021 Qian Yin et al. This is an open access article distributed under the Creative Commons Attribution License, which permits unrestricted use, distribution, and reproduction in any medium, provided the original work is properly cited.

This study analyzes the spatiotemporal evolution characteristics of seepage through a large-scale rock mass containing a filling joint. Firstly, a conceptual model was established to characterize the geomechanical occurrence of a typical water-resistant slab adjacent to a water-bearing structure. Then, a special apparatus was developed to conduct a hydromechanical test of a 3D large-scale rock mass. For a certain boundary stress and inlet water pressure, the pore water pressure in the joint first experiences a dramatic increase before approaching a constant value, and the steady pore water pressure presents a linear decrease along the joint length. A water inrush phenomenon happens as a result of connected flowing channels induced by migration of fillings. Using the finite element of COMSOL multiphysics, the influences of filling joint permeability, matrix permeability, and joint thickness as well as the inlet water pressure on seepage evolution in the jointed rock mass were, respectively, investigated. The pore water pressure increases with all these factors, and the stable pressure values increase with the inlet water pressure but decrease along the joint length. The flow velocity undergoes an increase with both the joint permeability and inlet water pressure but presents constant values independent on the matrix permeability or joint thickness. The water pressure contour planes distributed along the flowing path generally transfer from a “long funnel” shape to a “short funnel” shape before reaching a series of parallel pressure planes perpendicular to the joint direction. By using the genetic algorithm, the coupling influences of these factors on the pore water pressure and flow velocity were investigated, and the decision parameters were optimized. The calculated values show a good agreement with the numerical results, indicating a good prediction of the seepage evolution through the filling joint.

## 1. Introduction

In general, major water conservancy projects under construction and planning in China are concentrated in mountainous canyons at the upper reaches of rivers, and the key point of railway and highway construction is also located in Chinese southwestern regions with unprecedentedly complex geological and hydrological conditions [1–5]. During the construction process of deeply buried long tunnels, geological hazards especially water inrush and mud outburst often occur as a

result of large burial depth, high water pressure, high geostress, and strong disturbance [6–8]. Additionally, widely distributed disaster-causing structures such as joints, complicated fracture networks, and underground water-bearing structures in surrounding rocks make it more prone to instability of structural plane and groundwater, which would then produce engineering disasters [9–15]. For example, due to complicated hydrogeological conditions along the diversion tunnel of the Jinping-II Hydropower Station (with the deepest buried depth of 2500 m and the highest water

pressure of 10 MPa) in China, during the excavation process, the maximum groundwater discharge is  $7.3 \text{ m}^3/\text{s}$ , and 12 points with an extra-large water inflow rate exceeding  $1.0 \text{ m}^3/\text{s}$  are monitored (Figures 1(a) and 1(b)). Besides, a total of 19 large-scale water inrush accidents occurred in the construction process of the Yesanguan Tunnel of Yiwan Railway, China, with the largest water bursting discharge of approximately  $1.5 \times 10^5 \text{ m}^3/\text{h}$ , unfortunately leading to 15 deaths, major economic losses, a construction delay of 2 years, and serious destruction of ecological environment (Figures 1(c) and 1(d)). Therefore, there is no doubt that water inrush geohazards pose a serious threat to the performance and safety of underground excavation projects [16–19].

In recent years, researches focused on the water inrush mechanisms and prediction and early warning of geological hazards, and disaster prevention and control measures of practical engineering have been extensively performed [1, 4, 9, 18, 20–25]. A lot of interesting findings have been identified. However, few studies have so far given insight into the seepage spatiotemporal evolution characteristics in a water-resistant slab. Thus, in order to evaluate the process of seepage evaluation and water inrush more intuitively, a generalized model was established (Figure 2). A water-bearing structure, taking a karst cave as an example, with a certain hydraulic pressure in the joints or rock matrix, is in front of the tunneling direction. Due to irreversible perturbations during tunnel excavation, as well as the influence of water pressure, fractures are initiated, propagated, and coalesced to generate complex fracture networks, which would then form abundant fluid flow channels and entail significant changes in the permeability of the water-resistant slab [11, 26–28]. Additionally, both original and induced fractures/joints in the rock mass are usually filled with weathered debris of rocks, later intrusions of mud, and other materials, playing a vital role in seepage evolution and overall permeability of the rock mass [14, 15, 29, 30], which has rarely been reported.

Thus, in this study, a simplified sketch model describing the geomechanical state of a water-resistant slab was established, as shown in Figure 2. Here, the water-resistant slab is ideally treated as a cuboid model applied with a boundary stress of  $\sigma_y$  and  $\sigma_z$  in the  $y$ - and  $z$ -directions in the water-proof strata, a water pressure  $P$  on the boundary neighboring the water-bearing structure, and the water pressure on the boundary adjacent to the free face of the tunnel excavation that is assumed to be zero [9, 18, 26]. Based on the model established above, a large-scale three-dimensional physical simulation testing system ( $300 \times 300 \times 900 \text{ mm} \times 2$ ) for water inrush disasters in a rock mass was self-developed, and experimental investigation on quantitative analysis of seepage evolution and water inrush process in a rock mass containing a single filling joint was conducted. Then, a number of numerical simulations on the spatiotemporal evolution of pore water pressure and flow velocity, as well as the flow streamline distribution were conducted by employing the finite element method of COMSOL multiphysics, with respect to various factors of joint permeability  $K_j$ , matrix permeability  $K_m$ , joint thickness  $b$ , and the inlet hydraulic pressure  $P$ . Finally, a genetic algorithm was

utilized to propose a prediction model identifying the coupling influences of those factors on the flowing characteristics of the filling joint.

## 2. 3D Large-Scale Seepage Test of Rock Mass Containing a Filling Joint

*2.1. Development of the Testing System.* The special apparatus for a three-dimensional large-scale seepage test of a rock mass is shown in Figure 3. This system is mainly equipped with the following four units:

- (1) *The main bearing structure of the model.* The main body structure consists of a constraint framework and a bearing pedestal. The constraint framework is characterized by a bearing structure with the shape of a square hole inside a circle, and is intensively welded by steel plates with high qualities. Three stiffeners are separately added in each direction in order to improve both the strength and stiffness. The internal bearing structure has a cuboid shape with an allowable model size of  $300 \times 300 \times 900 \text{ mm} \times 2$  (Figures 3(a)–3(c))
- (2) *A boundary stress loading system.* The stress loading system consists of a piston-type uniform pressure loader, a servo oil-source system, and a control system. The boundary stress in the  $y$ - and  $z$ -directions can be individually imposed on a rock mass, with a pressure range of 0–6.0 MPa and a loading accuracy of  $\pm 2.0\%$ . The split piston uniform pressure loader can achieve a better uniform load distribution (Figures 3(b) and 3(c))
- (3) *A gas-liquid composite water supply system.* The hydraulic system consists of a group of high-pressure nitrogen tanks and a water tank that can supply a constant water pressure (Figure 3(d)). Nine high-pressure nitrogen cylinders, which can be individually switched on/off and can supply a gas pressure of up to 9.0 MPa for each cylinder, are laid out in parallel. The water tank has a bulk volume of  $1.5 \text{ m}^3$ , a designed maximum hydraulic pressure of 2.0 MPa, and a pressure accuracy of  $\pm 5.0\%$ . During the test, water is fed into the model through the water tank that can supply a constant water head at any moment driven by the gas-liquid composite water supply system
- (4) *A data acquisition system and other auxiliary equipment.* The data acquisition system consists of a data acquisition instrument, a sensor power supply module, a circuit board, and a computer (Figure 3(e)). The acquisition instrument is a 32-channel intelligent network distributed data acquisition and processing analyzer, the INV306N-6260, with a maximum sampling rate of 204.8 kHz, which can be utilized to realize the real-time data acquisition, wave display, and spectrum analysis



FIGURE 1: Typical geological disasters of water burst in underground engineering.

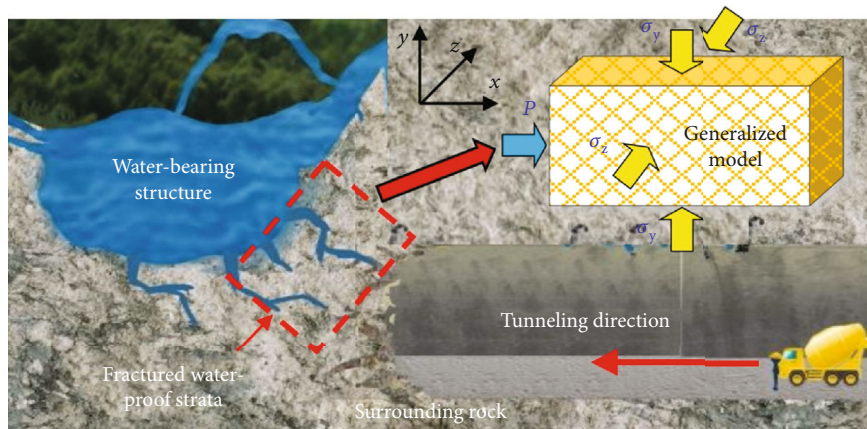


FIGURE 2: Schematic diagram of water inrush disaster in a typical underground project.

2.2. *Experimental Materials and Large-Scale Model Preparation.* During the test, cement and quartz sand were chosen as the main components to fabricate the matrix with a mass ratio of cement (C32.5 typical Portland cement), quartz sand (20–40 M), and water of 1 : 0.3 : 0.4. The joint was prefabricated and filled with dry and clean quartz sand.

First, samples of experimental materials were produced (Figure 4(a)) to conduct uniaxial compression (Figure 4(b)), Brazilian splitting, and variable angle shear tests (Figure 4(c)) to determine the basic mechanical properties of the cement mortar. The results indicate that after water curing of 7 days, average unit weight, uniaxial compressive



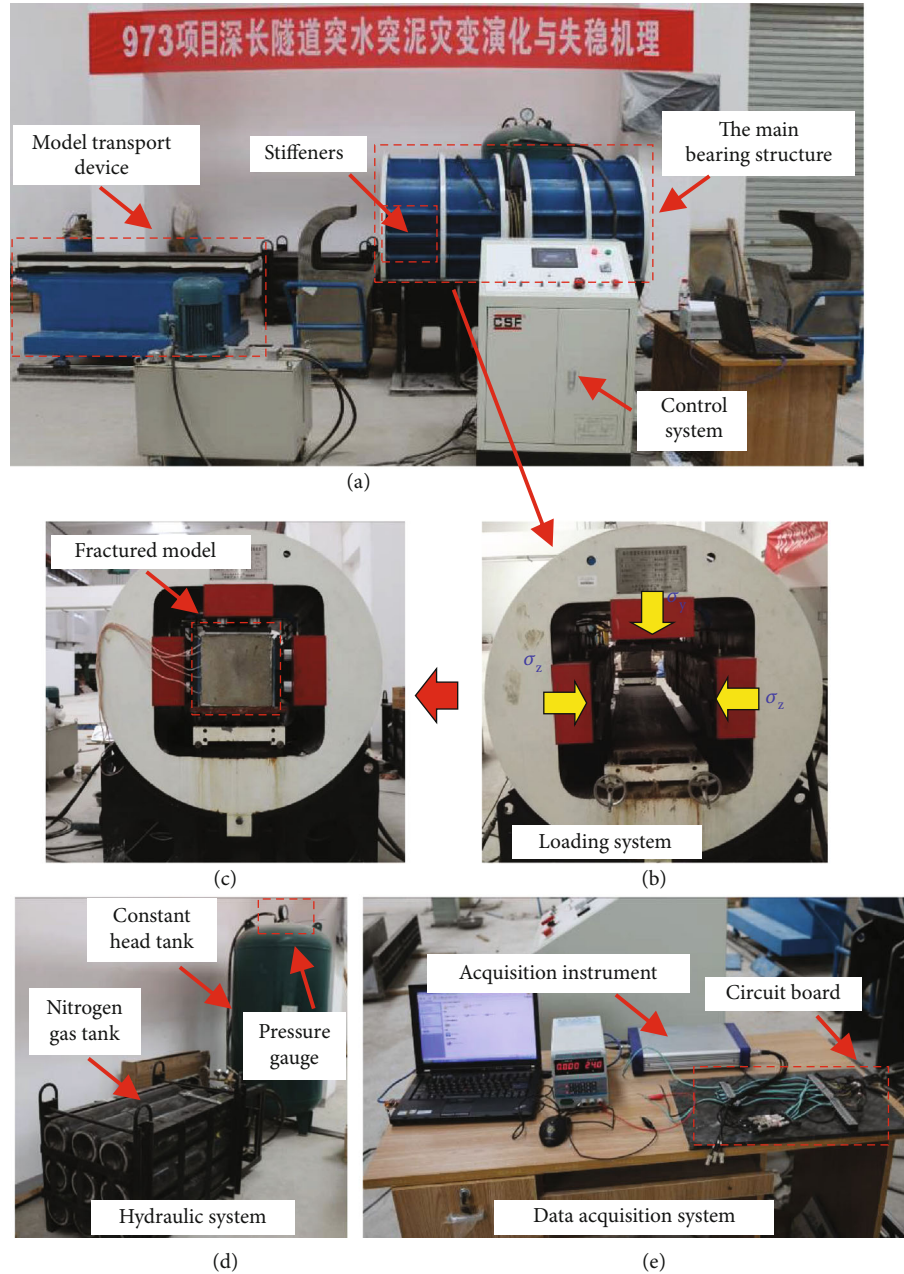


FIGURE 3: Large-scale three-dimensional fluid flow testing system.

strength, tensile strength, elastic modulus, cohesive force, and internal friction angle of the experimental materials are  $19.66 \text{ kN/m}^3$ ,  $2.85 \text{ MPa}$ ,  $0.29 \text{ MPa}$ ,  $0.32 \text{ GPa}$ ,  $0.61 \text{ MPa}$ , and  $31.22^\circ$ , respectively (Figure 4(d)). Additionally, with an increasing confining pressure from  $1.0$  to  $4.0 \text{ MPa}$ , permeability of the samples decreases from  $2.406 \times 10^{-10}$  to  $1.210 \times 10^{-10} \text{ m}^2$ .

The large-scale model containing a filling joint was poured by utilizing the method of layer filling and compaction, as follows:

- (1) Assemble the pouring mould (Figure 5(a)), clean the inner surface, and evenly apply a layer of lubricating oil. Prepare the water inlet device (Figure 5(b)). After

accurate weighing (Figure 5(c)) and stirring (Figure 5(d)), the experimental materials were poured into the mould laying in three times, respectively, with uniform vibration (Figure 5(e)). The height of each filled layer was  $10 \text{ mm}$

- (2) During the pouring process, the joint with a length of  $900 \text{ mm}$ , width of  $100 \text{ mm}$ , and thickness of  $10 \text{ mm}$  was prefabricated. Thus, the water inlet device was embedded in the middle position of the model in the second layer (Figure 5(f)). After the joint was produced (Figure 5(g)), clean quartz sand was filled (Figure 5(h)), and five high-precision WMS-51 micro water pressure sensors with a pressure range of  $0$ –



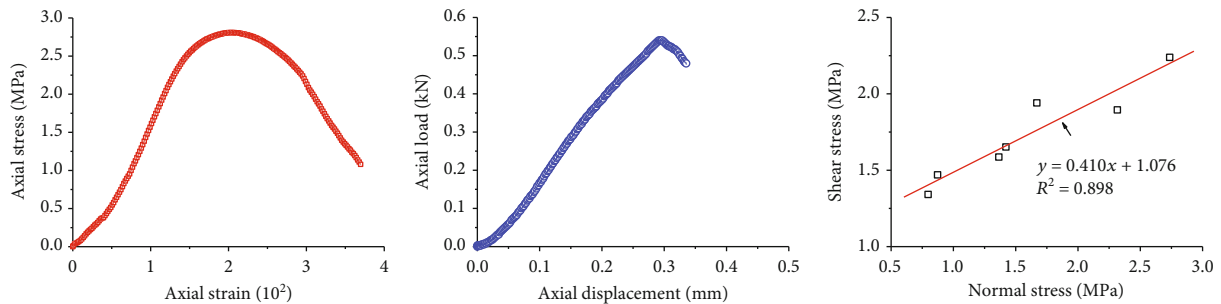
(a) Sample preparation



(b) Uniaxial compression test



(c) Brazilian splitting and variable angle shear tests



(d) Stress-strain curves in the uniaxial compression, Brazilian splitting, and angle shear tests

FIGURE 4: Experimental materials and basic mechanical tests.

2.5 MPa and an accuracy of 0.5% were embedded in the joint along a length-wise direction with a spacing of 160 mm (Figure 5(i))

**2.3. Sealing and Installation of the Large-Scale Model.** After completion of the model pouring, the model was made to stand up in a length-wise direction, demoulded, and cured for 7 days. Then, a layer of epoxy resin was evenly applied on the model surface (Figure 5(j)) and a layer of crack-

resistant seam belt was timely wrapped to bond together with the epoxy resin (Figure 5(k)). After the epoxy resin was solidified after 24 h, a layer of polyurethane was applied on the crack-resistant seam belt (Figure 5(l)). When the polyurethane was solidified after 48 h, the above steps were repeated once again. Finally, the model surface was cleaned, especially the bottom position at which some waste sealing materials may be piled up (Figure 5(m)), and a knife was utilized to cut through the waterproof boundary at the position of the

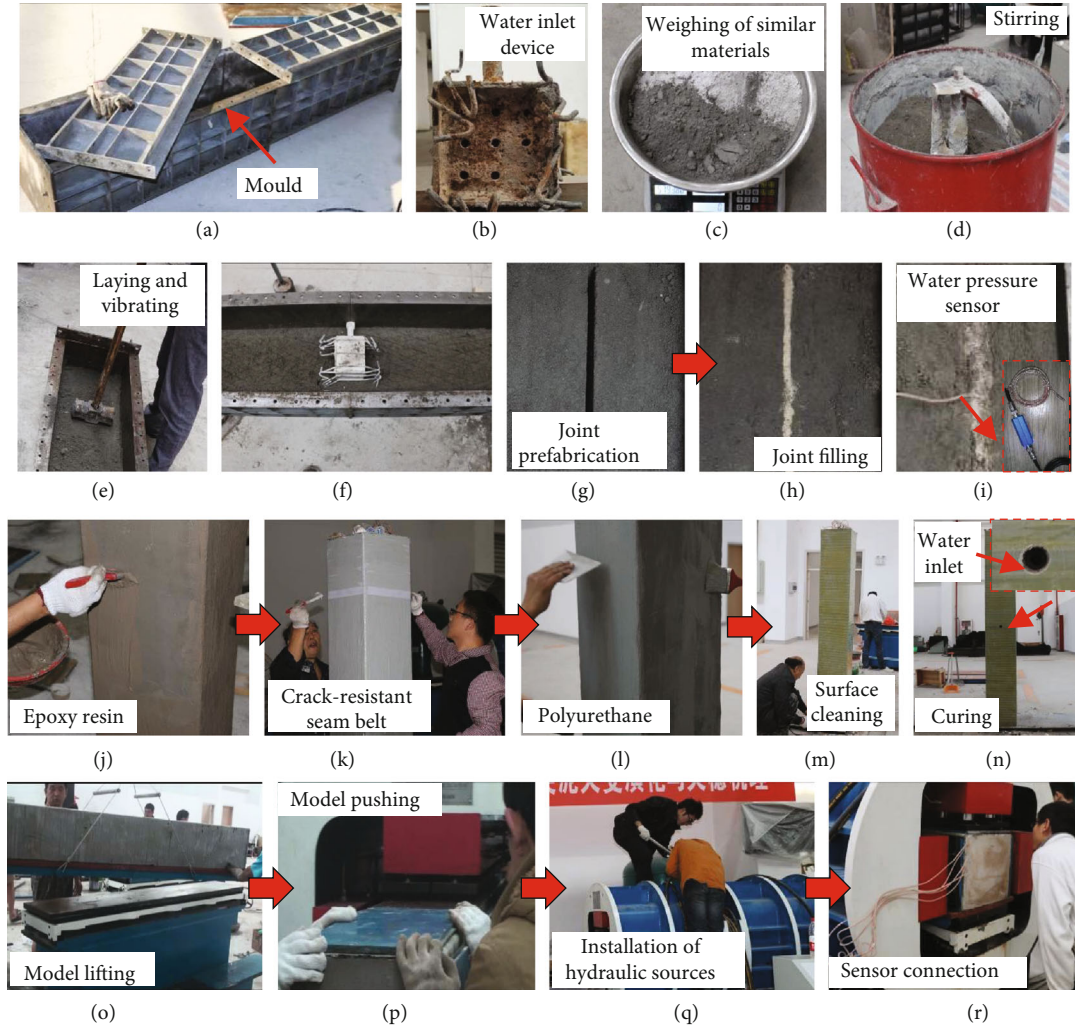


FIGURE 5: A typical process of model pouring, sealing, and installation.

embedded water inlet device, from which the model can be connected with the hydraulic system (Figure 5(n)).

The sealed rock mass containing a single filling joint was then placed on a bearing platform with the connector of the water inlet device upwards, and the model was carefully lifted by pushing and the device was precisely positioned using a hoist (Figure 5(o)). Then, the model was pushed into the test system, the end of the model was aligned with loading system boundary (Figure 5(p)), and the water inlet device was connected with the gas-liquid composite water supply system using a rubber pipe (Figure 5(q)). Finally, the lead wires of the water pressure sensors were connected with the data acquisition system (Figure 5(r)), debugged, and the initial values cleared.

**2.4. Test Procedure, Results, and Discussion.** The schematic diagram of the rock mass containing a filling joint, gas-liquid composite water supply system, water inlet device, and embedding arrangement of the water pressure sensors is displayed in Figure 6. Note that in the experiment, we just focused on half of the model, with the joint (the length of 900 mm) located at the exact central position of the matrix.

In addition, a gravel filter was arranged between the water inlet device and the joint to achieve a uniform distribution of water pressure and prevent the water inlet device being blocked. By using a hydraulic access, variable but uniform inlet water pressures can be applied to the rock mass.

During the test, both boundary stresses in the  $y$ - and  $z$ -directions were constant at 5 MPa, and the inlet water pressure  $P$  was set to be 0.3 MPa. Then, variations in the pore water pressure  $p$  with time ( $t = 0\text{--}2500$  s) and the joint length ( $L = 60, 220, 380, 540, 700$  mm) can be analyzed. Figure 7(a) presents the spatiotemporal evolution characteristics of  $p$ . It can be seen that the pore water pressure at all the five positions through the filling joint shows an increase with  $t$ . At the beginning,  $p$  changes significantly with  $t$ . However, as  $t$  continuously increases, the increasing rate steadily diminishes and  $p$  gradually approaches a constant value. The variation of  $p$  as a function of  $t$  can be well described using an exponential function. In addition, the variation rate of  $p$  at various positions along the joint is different, indicating a larger value for the position close to the water inlet. For  $t = 2500$  s, the constant  $p$  values for the measure points E\_#1, E\_#2, E\_#3, E\_#4, and E\_#5 are 0.2767, 0.2097, 0.1450,



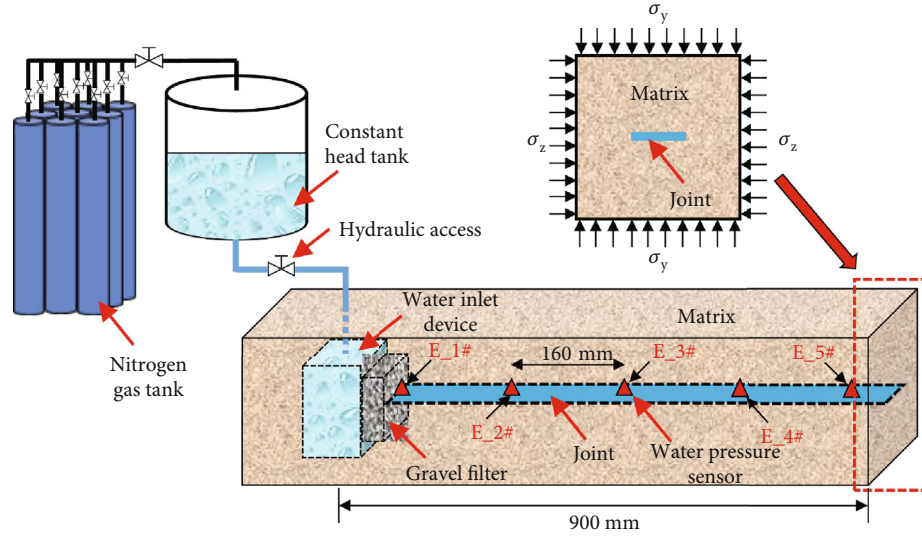


FIGURE 6: Schematic diagram of the water supply system and embedding location of the water pressure sensors.

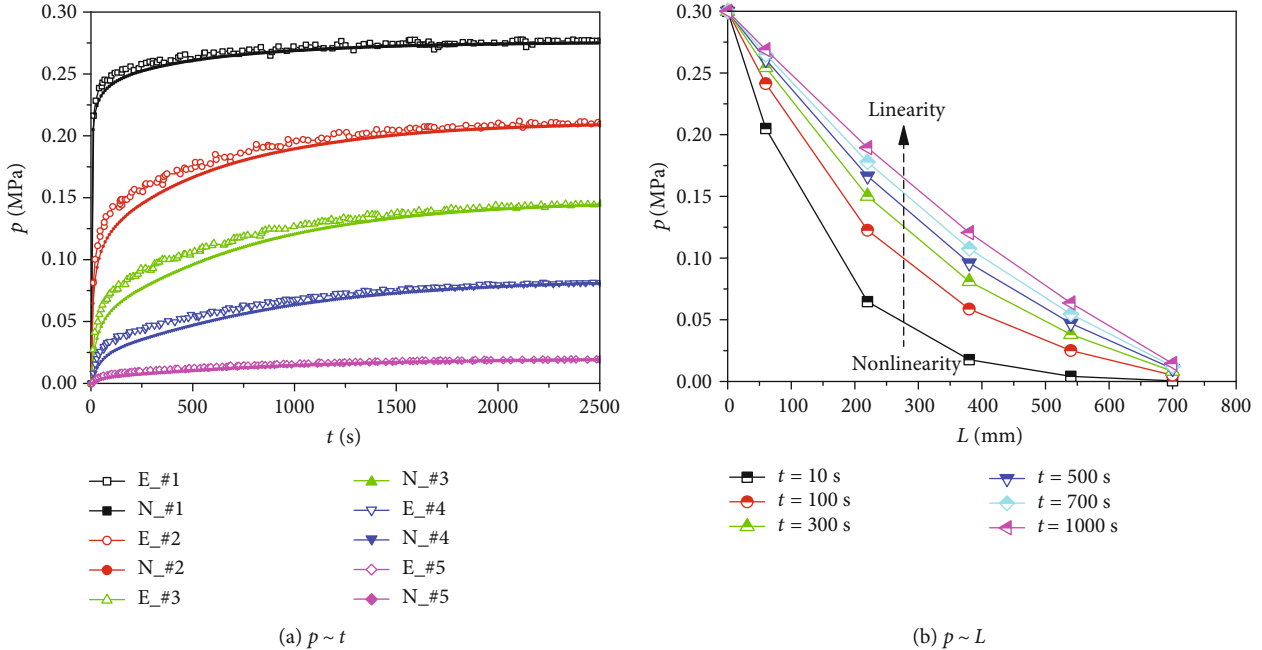


FIGURE 7: Experimental and numerical evolution characteristics of  $p$ .

0.0815, and 0.0195 MPa, respectively, showing a decrease of 92.95% for the water pore pressure along the joint length. Besides, at a small  $t$  (e.g.,  $t = 100, 300$  s), the decrease in  $p$  with  $L$  presents a nonlinear trend. With increasing  $t$  ( $t = 1000$  s), the variation trend of  $p$  versus  $L$  gradually transfers from nonlinearity to linearity (Figure 7(b)).

As the inlet water pressure is continually applied, the filling materials are dissolved in water and carried away by water with time. Connected fluid flowing channels are gradually produced in the filling joint, and a water inrush phenomenon from the joint occurs at the model boundary, as shown in Figure 8. Besides, this is due to the fact that the flow capacity of the matrix is several orders of magnitude

smaller than that of the filling joint. The matrix surface of the model is just wet, which indicates slight leakage rather than significant flow streamlines.

### 3. Finite Element Analysis of Seepage Evolution in a Filling Joint

3.1. Numerical Simulation Schemes. As a result of complex operation, heavy workload, and long time consumed by a large-scale physical model test, a large number of experimental studies with multivariables are difficult to achieve. Thus, here, we applied the finite element analysis software COMSOL multiphysics [1, 4, 31–33] to evaluate the seepage

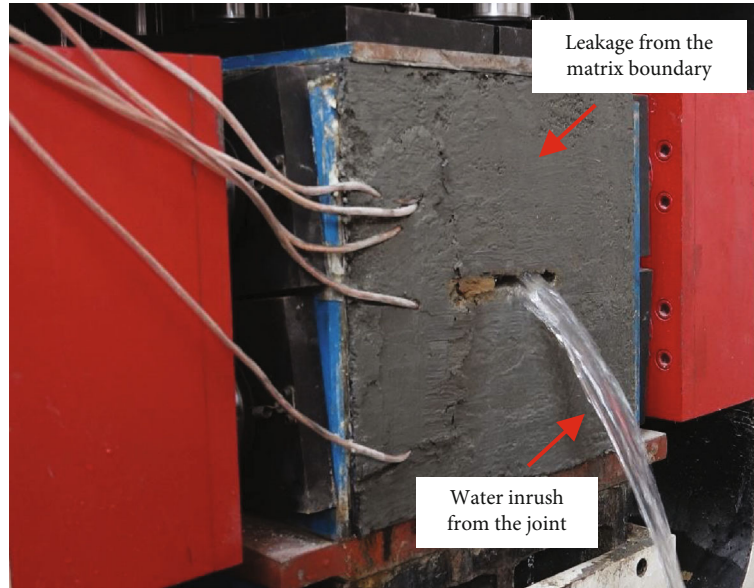


FIGURE 8: Water seepage characteristics at the model boundary.

evolution in the filling joint. Here, both the numerical model size and boundary conditions are consistent with the large-scale physical model test (Figure 9). The module of fracture flow was chosen, and the governing equations of fluid flow through the large-scale rock mass with a filling joint are the well-known Navier-Stokes (NS) equations and mass and momentum conservations, as follows:

$$\begin{aligned} \nabla \cdot \mathbf{u} &= 0, \\ \rho(\mathbf{u} \cdot \nabla)\mathbf{u} - \mu \nabla^2 \mathbf{u} + \nabla P &= 0, \end{aligned} \quad (1)$$

where  $\rho$  (kg/m<sup>3</sup>),  $\mathbf{u}$  (m/s),  $P$  (Pa),  $\mu$  (Pa · s), and  $t$  (s) denote the density of a fluid, the velocity vector, the pressure, the viscosity coefficient, and time, respectively.

The numerical model has a total of 105,261 microelements, and the whole calculation process of fluid flow took approximately 1.2 hours by using a personal computer with an i7 core. To determine the micro seepage parameters of the numerical model, a “trial and error” method was utilized by calibrating the porosity and permeability of both the matrix and the filling joint. All the micro input parameters which were finally confirmed for the numerical model are listed in Table 1. Note that due to the much larger size of the model compared to the aperture thickness of the joint, the boundary effects of the three-dimensional model were ignored here in this study. Figure 7(a) presents the comparison between the numerically simulated and experimental variations in pore water pressures, which exhibits a good agreement for the  $p \sim t$  curves. Based on the above micro numerical simulation parameters, the influences of permeability of filling joints ( $K_j = 2 \times 10^{-10}$ ,  $4 \times 10^{-10}$ ,  $6 \times 10^{-10}$ ,  $8 \times 10^{-10}$ , and  $10 \times 10^{-10}$  m<sup>2</sup>), permeability of matrix ( $K_m = 2 \times 10^{-12}$ ,  $4 \times 10^{-12}$ ,  $6 \times 10^{-12}$ ,  $8 \times 10^{-12}$ , and  $10 \times 10^{-12}$  m<sup>2</sup>), joint thickness ( $b = 2, 4, 6, 8,$  and  $10$  mm), and inlet water pressure ( $P = 0.1, 0.3, 0.5, 0.7,$  and  $0.9$  MPa) on

evolution characteristics of the pore water pressure, flow velocity, and flow streamline distribution were investigated, respectively. The variable-controlling approach was adopted, and a total of 17 numerical models were established, as listed in Table 2.

**3.2. Dynamic Evolution Process of the Pore Water Pressure.** Variations in  $p$  for a rock mass containing a filling joint with respect to various  $K_j$ ,  $K_m$ ,  $b$ , and  $P$  values in the  $t$  range of 0–3600 s are displayed in Figure 10, in which, the measuring points at  $L = 0.1, 0.3, 0.5,$  and  $0.7$  m were chosen, respectively. As  $t$  increases,  $p$  presents an increasing trend, first indicating a remarkable increase and then reaching a stable value, which can be well characterized using an exponential function. Generally, the increase rate of  $p$  declines.

Figures 10(a)–10(c), respectively, show the variations in  $p$  in terms of various  $K_j$ ,  $K_m$ , and  $b$  values. At the initial loading stage of water pressure, a smaller  $K_j$ ,  $K_m$ , or  $b$  value will result in a smaller  $p$  value at the same position in the filling joint. However, when  $p$  reaches stable values, the pore water pressure for an identical  $L$  is generally the same, which is independent on  $K_j$ ,  $K_m$ , or  $b$ . For  $t = 3600$  s, the stable  $p$  values for  $L = 0.1, 0.3, 0.5$  and  $0.7$  m are 0.26, 0.17, 0.09, and 0.02 MPa, respectively, indicating a generally linear decrease of 92.31% along the joint length. The above variation trends of  $p$  are attributed to the same inlet water pressure  $P$ , due to the fact that the pore water pressure in steady states are just affected by the applied inlet water pressure. In order to explore the influences of  $P$  on the evolution of pore water pressures, fluid flow simulations on a jointed rock mass with  $P = 0.1, 0.3, 0.5, 0.7,$  and  $0.9$  MPa were conducted (Figure 10(d)). For a certain  $L$ , as  $P$  increases, the stable  $p$  exhibits an increase. Taking  $L = 0.3$  m as an example, in the  $P$  range of 0.1–0.9 MPa, the pore water pressure increases from 0.060 to 0.538 MPa, or by a factor of 7.97.



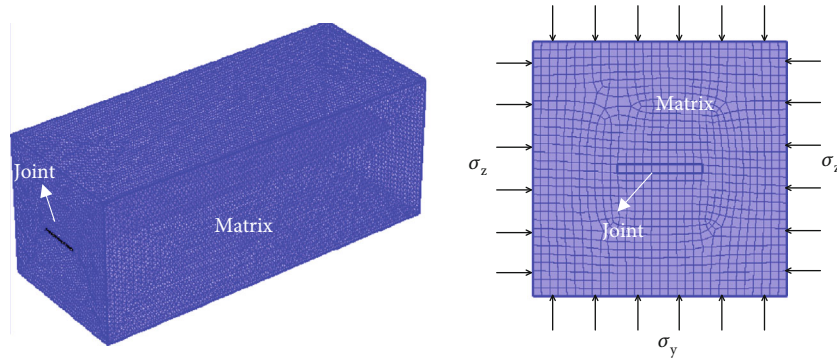


FIGURE 9: Finite element model using COMSOL multiphysics.

TABLE 1: Microparameters of the numerical model in the simulation.

$K_j$ ( $10^{-10} \text{ m}^2$ )	$K_m$ ( $10^{-12} \text{ m}^2$ )	$b$ (mm)	$n_m$	$n_j$	$P$ (MPa)	$\mu$ ( $10^{-3} \text{ Pa}\cdot\text{s}$ )
8	2	10	0.20	0.45	0.3	1

Note:  $K_j$  = permeability of joint;  $K_m$  = permeability of matrix;  $b$  = joint thickness;  $n_m$  = porosity of matrix;  $n_j$  = porosity of joint;  $P$  = inlet water pressure;  $\mu$  = dynamic viscosity of water.

TABLE 2: Numerical simulation conditions in this study.

Model	$K_j$ ( $10^{-10} \text{ m}^2$ )	$K_m$ ( $10^{-12} \text{ m}^2$ )	$b$ (mm)	$P$ (MPa)	Note
#1	2				
#2	4				
#3	6	2	10	0.3	Various $K_j$
#4	8				
#5	10				
#6		2			
#7		4			
#8	8	6	10	0.3	Various $K_m$
#9		8			
#10		10			
#11			2		
#12			4		
#13	8	2	6	0.3	Various $b$
#14			8		
#15			10		
#16				0.1	
#17				0.3	
#18	8	2	10	0.5	Various $P$
#19				0.7	
#20				0.9	

3.3. Attenuation Characteristics of the Pore Water Pressure along Joint Length. Similar to the large-scale model test results, for a certain  $t$ , the numerically simulated  $p$  shows an attenuation along the flowing paths (Figure 11). At the initial stage of fluid flow (e.g.,  $t = 100, 300,$  and  $500$  s), the pore water pressure shows an obvious nonlinear decrease along the flowing path, indicating a concave shape. However, as  $t$

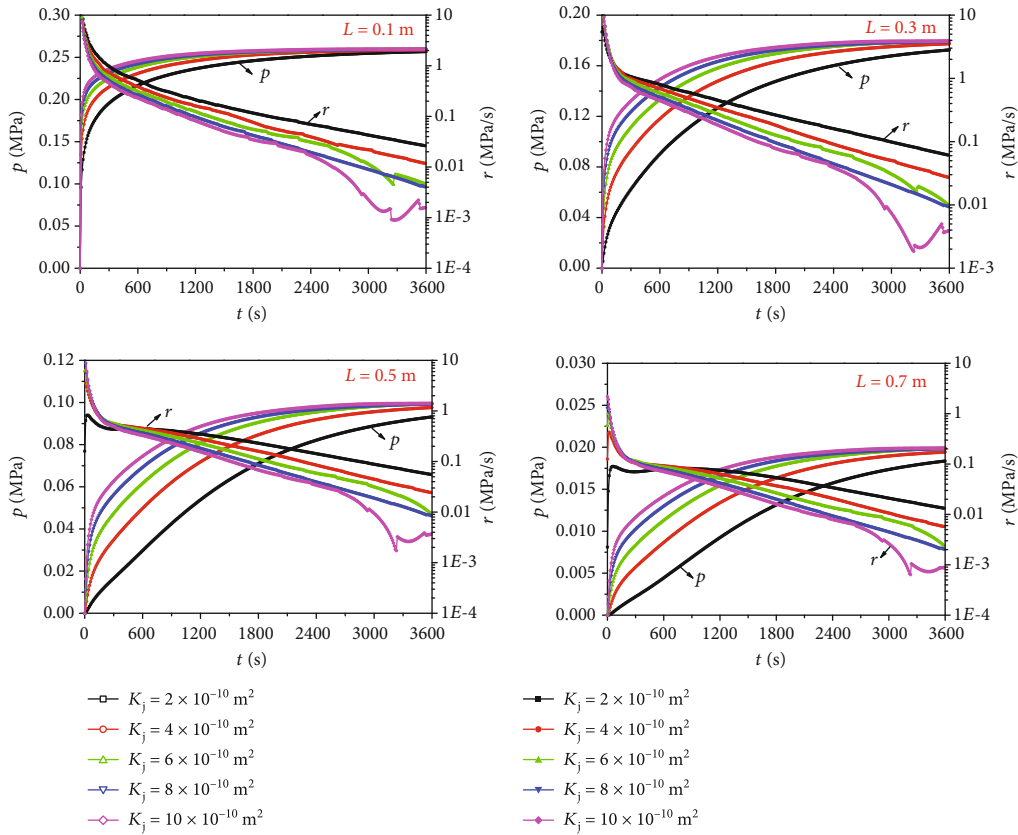
increases, nonlinear characteristics of the  $p \sim L$  curves weaken while the linearity enhances. At  $t = 1000$  s, the variation in  $p$  with  $L$  has generally transferred to a linear decrease. From Figure 11(a), nonlinear characteristics of  $p$  against  $L$  are more obvious for a smaller  $K_j$ , with a larger curvature of the  $p \sim L$  curves, which will take longer for the transition of the curves from nonlinearity to linearity. Compared with  $K_j$ , the permeability of matrix  $K_m$  has little influence on  $p$  distributions along the joint (Figure 11(b)). From Figure 11(c), the pore water pressure is larger for a larger joint thickness in the early fluid flowing stage, and the nonlinearity of the  $p \sim L$  curves is more obvious for a small  $b$  value. In the steady flowing state, the  $p$  value is independent on  $b$ , indicating a linear decrease with  $L$ . Figure 11(d) presents the transition of  $p$  distributions for the jointed rock mass with various  $P$ . Clearly, at  $t = 1000$  s, the  $p \sim L$  curve exhibits an increasing reduction rate with  $P$ .

Generally, from Figure 11, attenuation characteristics of  $p$  with  $L$  can be well described using a negative exponential function, as follows:

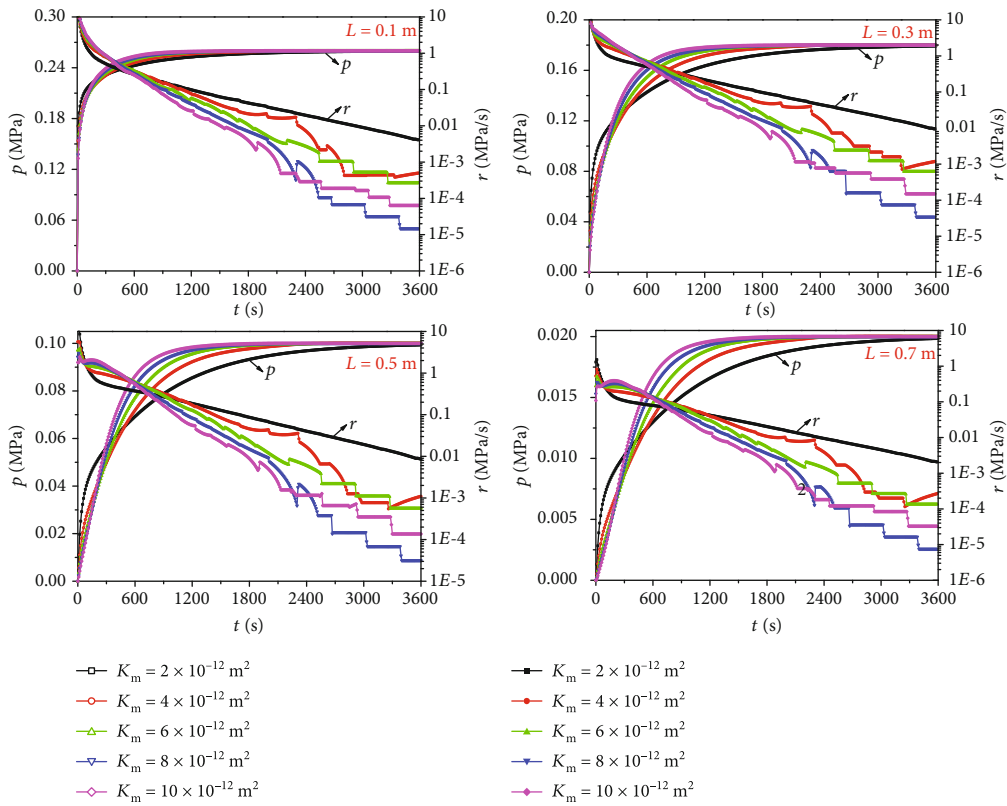
$$p = \frac{e^{(-AL+B)} + C}{e^B + C} \times P, \quad (2)$$

where  $A, B,$  and  $C$  are fitting coefficients, which are related with  $K_j, K_m, b,$  and  $P$ .

Figure 12, respectively, shows the variations in coefficient  $A$  with  $K_j, K_m, b,$  and  $P$ . As  $K_j$  increases,  $A$  shows a decrease. Taking  $t = 500$  s as an example,  $A$  decreases from 3.586 to 1.279, by 64.33% in the  $K_j$  range of  $2 \times 10^{-10}$  to  $10 \times 10^{-10} \text{ m}^2$ . Coefficient  $A$  first increases then decreases with  $K_m$ . In the  $b$  range of 2–10 mm,  $A$  shows a decrease from 3.855 to 1.538, by 60.10% at  $t = 500$  s. However, coefficient  $A$  keeps constant in the  $P$  range of 0.1–0.9 MPa.

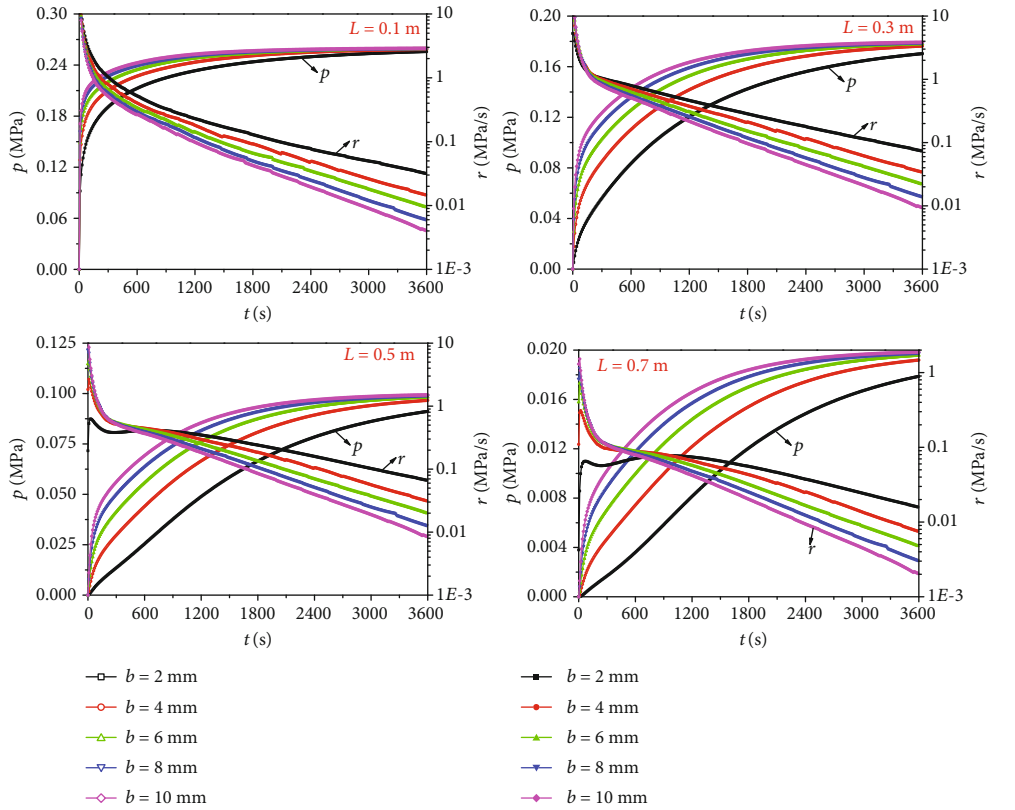


(a)  $K_m = 2 \times 10^{-12} \text{ m}^2$ ,  $b = 10 \text{ mm}$ ,  $P = 0.3 \text{ MPa}$ , various  $K_j$

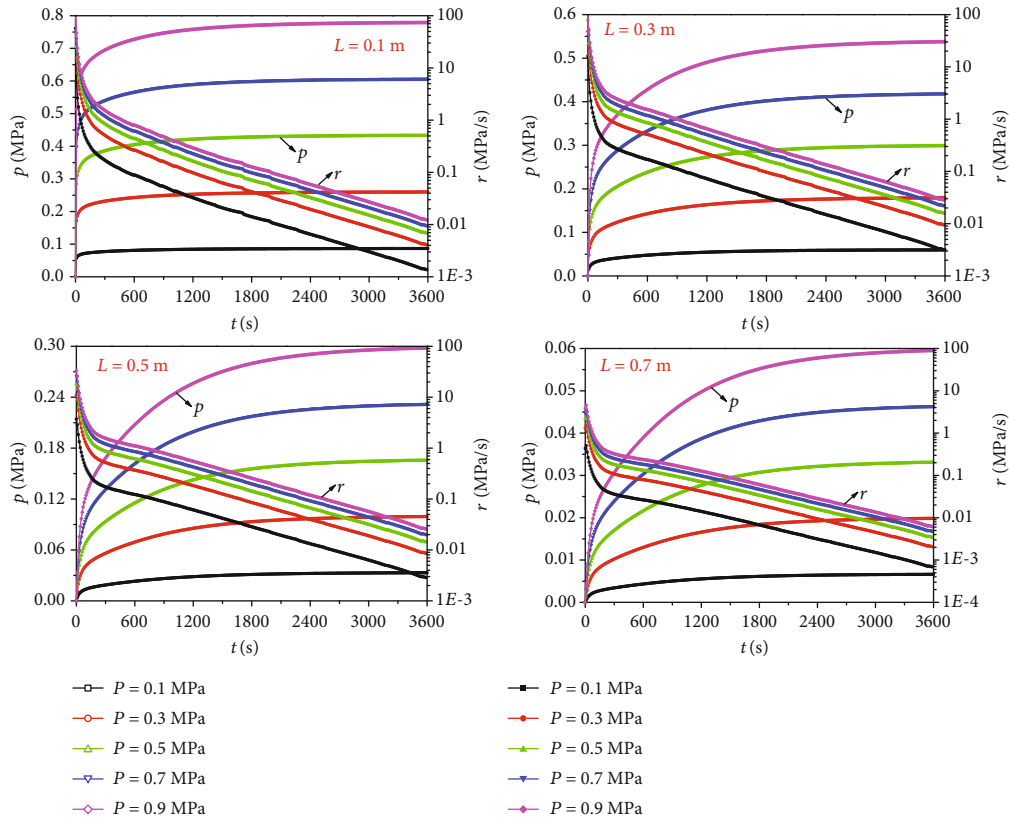


(b)  $K_j = 8 \times 10^{-10} \text{ m}^2$ ,  $b = 10 \text{ mm}$ ,  $P = 0.3 \text{ MPa}$ , various  $K_m$

FIGURE 10: Continued.



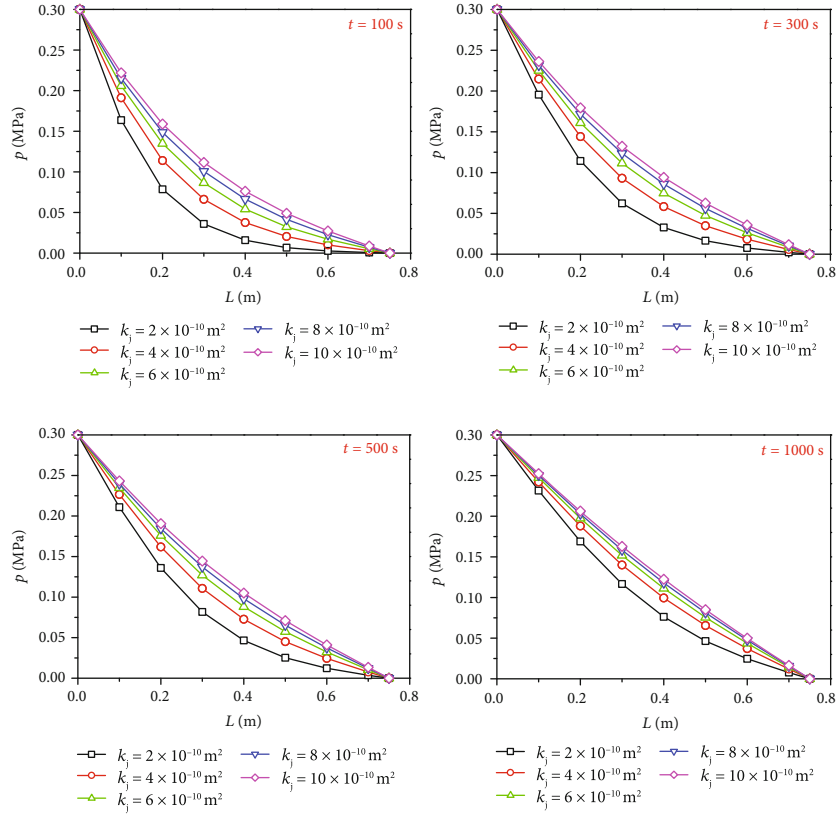
(c)  $K_j = 8 \times 10^{-10} \text{ m}^2$ ,  $K_m = 2 \times 10^{-12} \text{ m}^2$ ,  $P = 0.3 \text{ MPa}$ , various  $b$



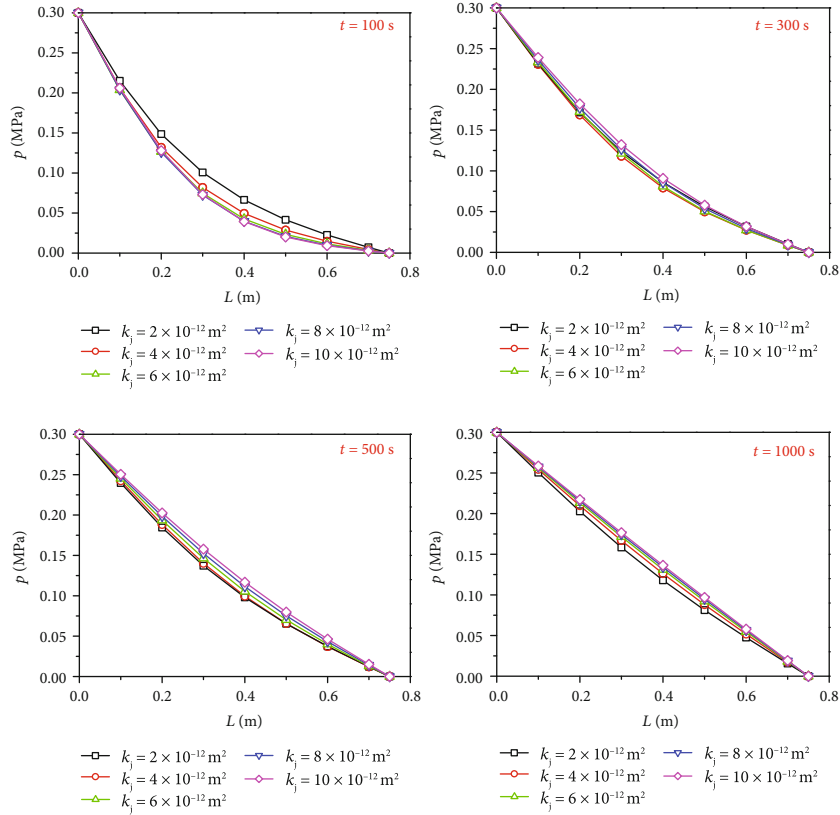
(d)  $K_j = 8 \times 10^{-10} \text{ m}^2$ ,  $K_m = 2 \times 10^{-12} \text{ m}^2$ ,  $b = 10 \text{ mm}$ , various  $P$

FIGURE 10: Variations in  $p$  with respect to various  $K_j$ ,  $K_m$ ,  $b$ , and  $P$ .



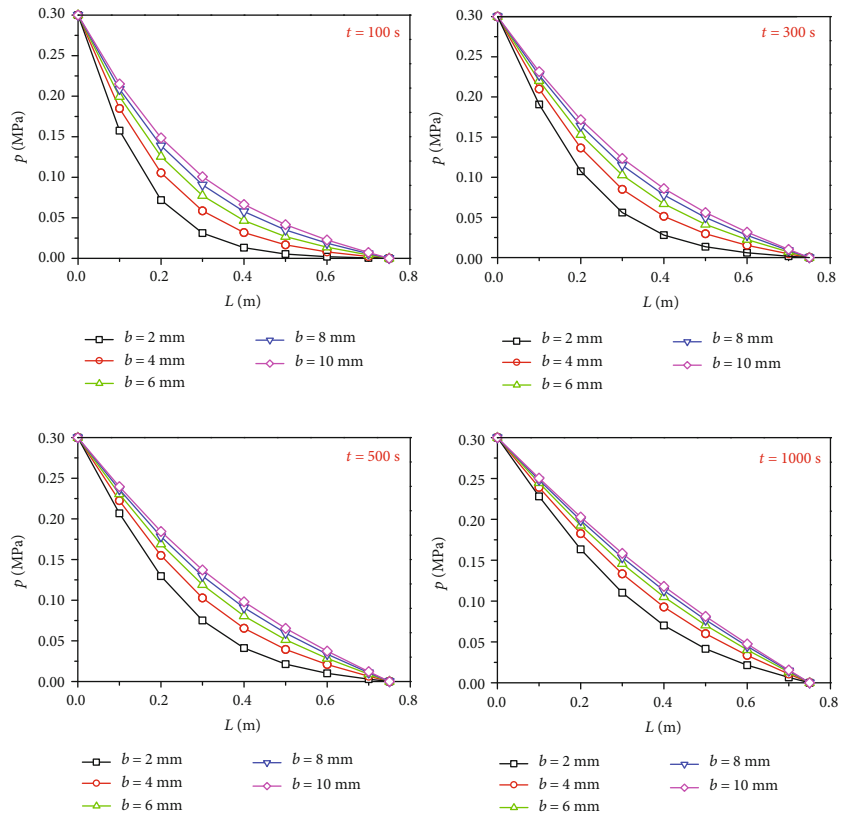


(a)  $K_m = 2 \times 10^{-12} \text{ m}^2$ ,  $b = 10 \text{ mm}$ ,  $P = 0.3 \text{ MPa}$ , various  $K_j$

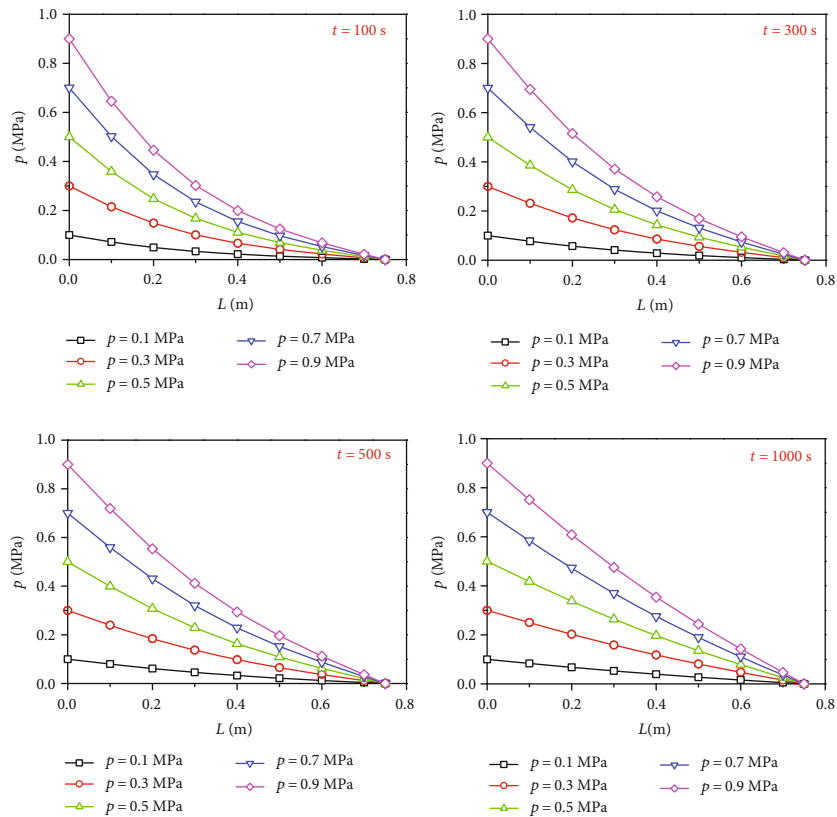


(b)  $K_j = 8 \times 10^{-10} \text{ m}^2$ ,  $b = 10 \text{ mm}$ ,  $P = 0.3 \text{ MPa}$ , various  $K_m$

FIGURE 11: Continued.



(c)  $K_j = 8 \times 10^{-10} \text{ m}^2$ ,  $K_m = 2 \times 10^{-12} \text{ m}^2$ ,  $P = 0.3 \text{ MPa}$ , various  $b$



(d)  $K_j = 8 \times 10^{-10} \text{ m}^2$ ,  $K_m = 2 \times 10^{-12} \text{ m}^2$ ,  $b = 10 \text{ mm}$ , various  $P$

FIGURE 11: Numerical results and corresponding fitting curves of  $p$  versus  $L$  under different conditions.

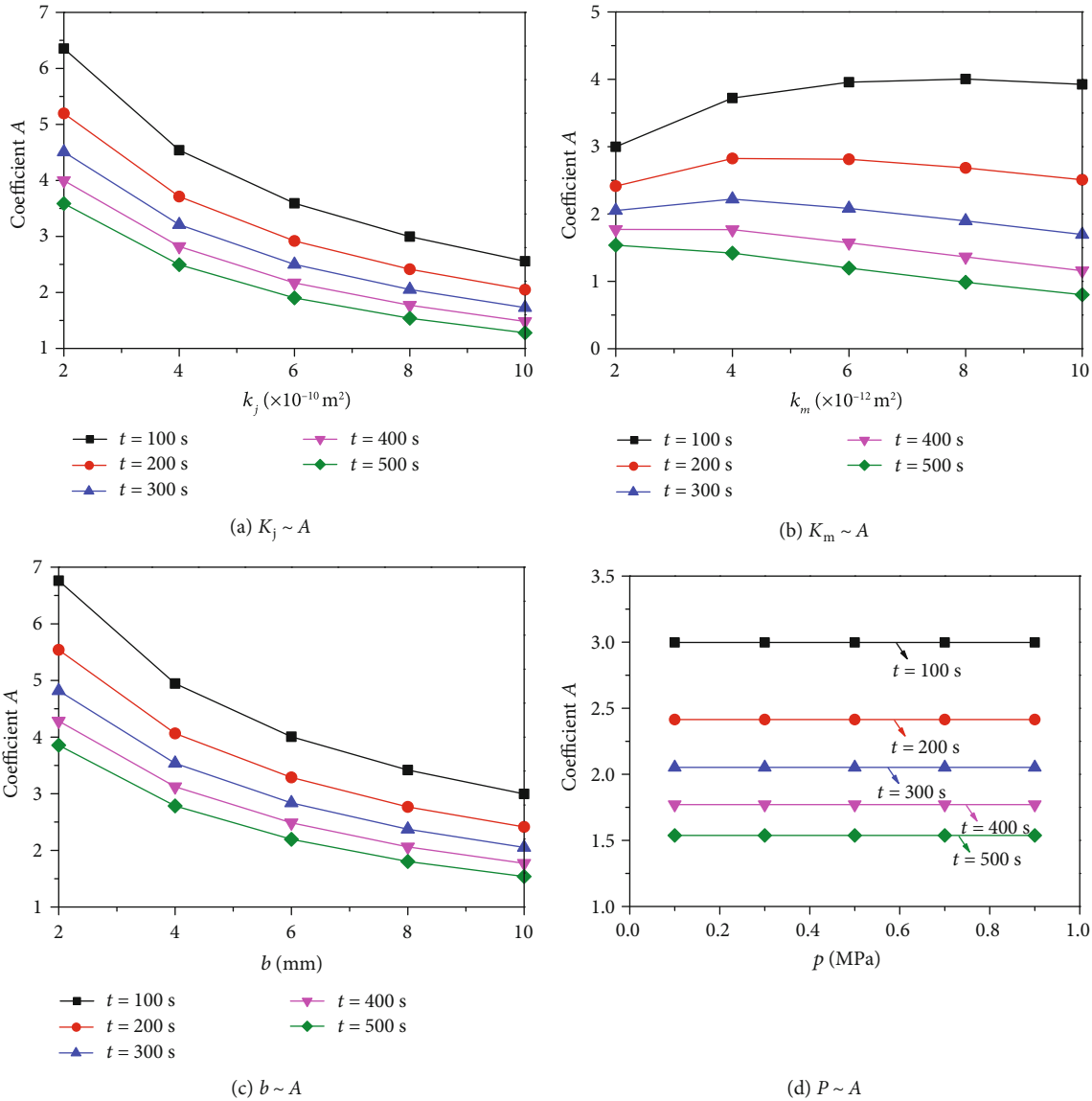


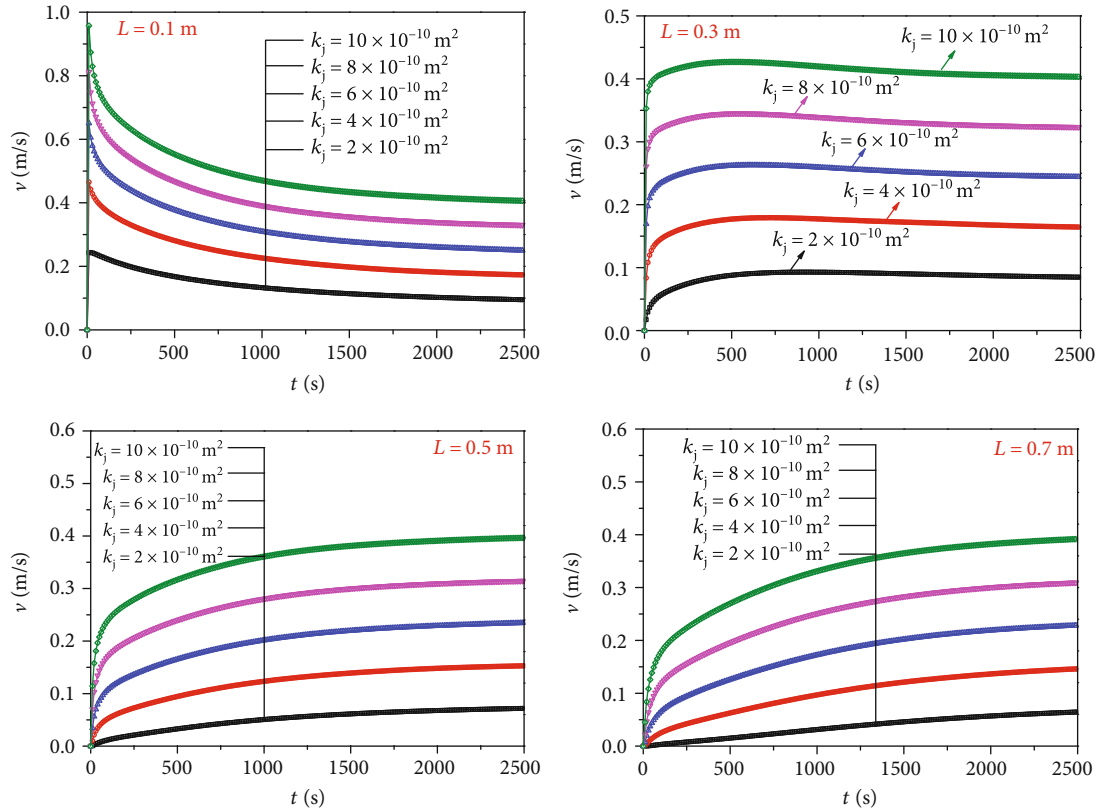
FIGURE 12: Variations in coefficient  $A$  with respect to different  $K_j$ ,  $K_m$ ,  $b$ , and  $P$ .

**3.4. Variations in the Flow Velocity.** Figure 13 presents the changes in flow rate  $v$  in the joint with respect to various  $K_j$ ,  $K_m$ ,  $b$ , and  $P$ . It can be seen that, from Figures 13(a) and 13(d), after the water pressure was applied, the flow velocity will occupy a larger value for the measure points in the joint with a larger  $K_j$  or  $P$ . When fluid flowing attains an equilibrium state, with increasing  $K_j$  or  $P$ , the steady  $v$  in the joint shows an increase. Taking  $L = 0.7$  m in Figure 13(a) as an example, in the  $K_j$  range of  $2 \times 10^{-10}$  to  $10 \times 10^{-10}$  m<sup>2</sup>,  $v$  increases by a factor of 4.42. Additionally, at a small joint length (e.g.,  $L = 0.1$  and  $0.3$  m), the flow velocity first increases and then decreases with  $t$ , but for a large joint length ( $L > 0.3$  m),  $v$  experiences a monotonous increase with  $t$  before it approaches a constant value in the steady flowing state. From Figures 13(b) and 13(c), for  $L = 0.1$  and  $0.3$  m, the flow velocity presents at first an increasing and then a

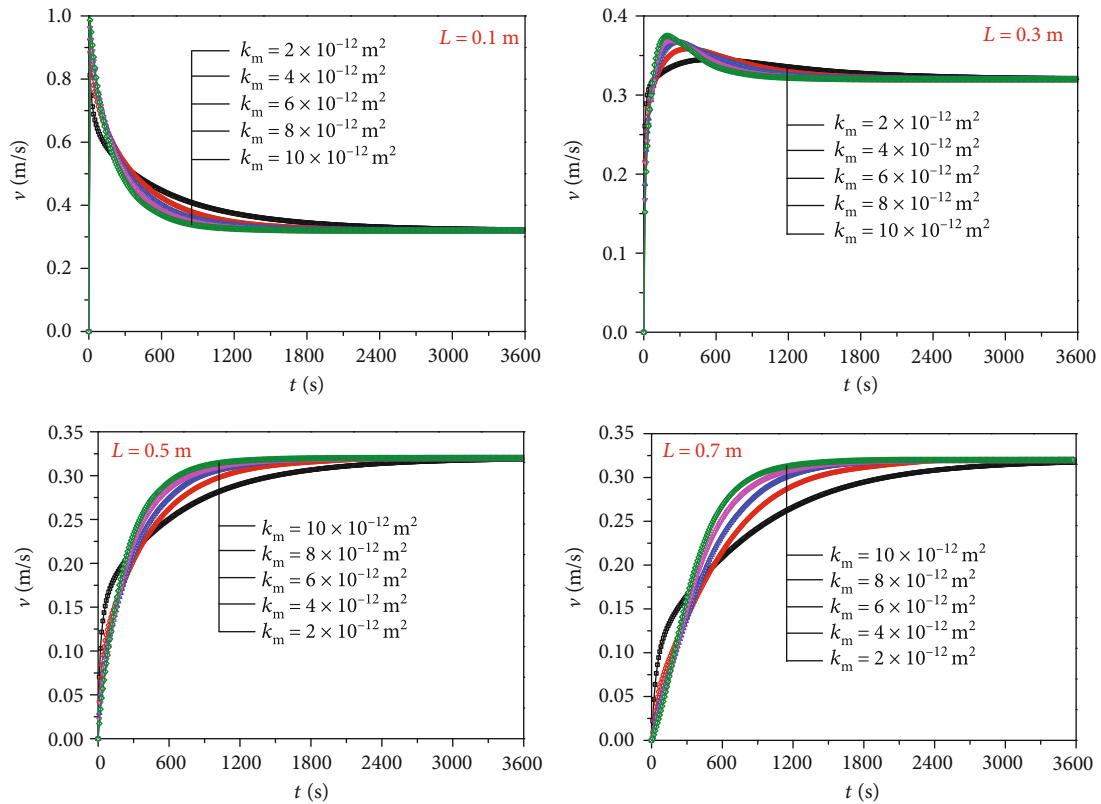
decreasing trend, but for  $L = 0.5$  and  $0.7$  m,  $v$  shows an increase until the steady states. In the steady state, the flow velocity is a constant value independent of  $K_m$  or  $b$ .

Figure 14 shows the water pressure contour planes and flow streamlines through the jointed rock mass with various  $K_j$ ,  $K_m$ ,  $b$ , and  $P$ . At the initial fluid flow stage, distribution of pore water pressure presents a “long funnel” shape, which is due to the larger  $K_j$  than  $K_m$ . The diffusion velocity of pore water pressure in the joint is greater than that in the matrix, and fluid flow first reaches the boundary of the model through the joint before it spreads to the whole model end boundary, which is generally consistent with the physical test results in Figure 8. Then, with increasing  $t$ , the water pressure contour plane gradually transfers from a “long funnel” to a “short funnel” shape. When the water pressure distribution is steady, the pressure isosurfaces



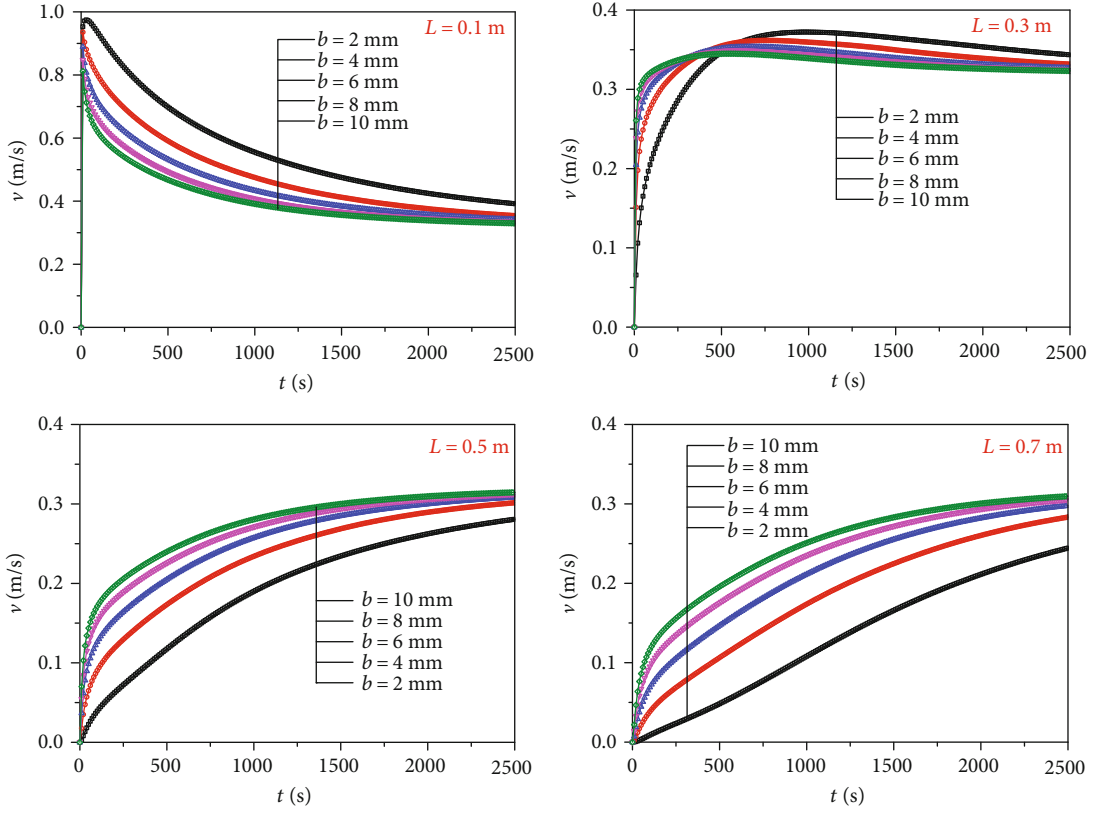


(a)  $K_m = 2 \times 10^{-12} \text{ m}^2$ ,  $b = 10 \text{ mm}$ ,  $P = 0.3 \text{ MPa}$ , various  $K_j$

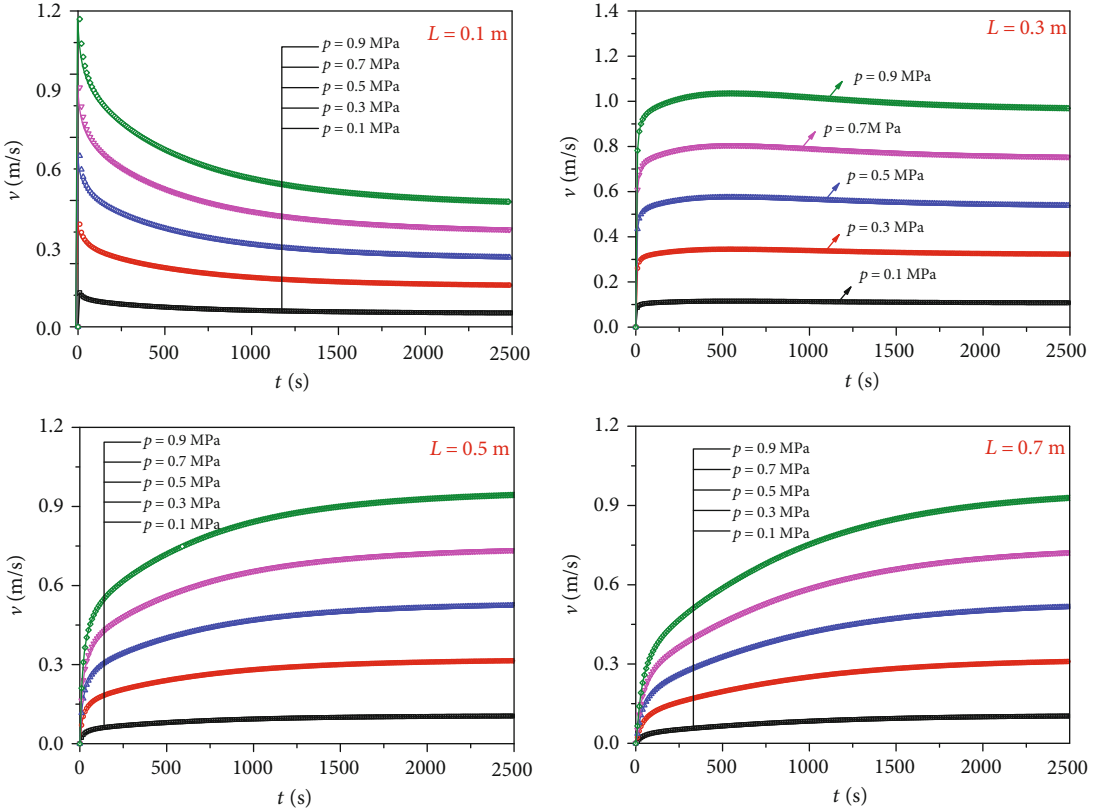


(b)  $K_j = 8 \times 10^{-10} \text{ m}^2$ ,  $b = 10 \text{ mm}$ ,  $P = 0.3 \text{ MPa}$ , various  $K_m$

FIGURE 13: Continued.



(c)  $K_j = 8 \times 10^{-10} \text{ m}^2$ ,  $K_m = 2 \times 10^{-12} \text{ m}^2$ ,  $P = 0.3 \text{ MPa}$ , various  $b$



(d)  $K_j = 8 \times 10^{-10} \text{ m}^2$ ,  $K_m = 2 \times 10^{-12} \text{ m}^2$ ,  $b = 10 \text{ mm}$ , various  $P$

FIGURE 13: Changes in flow rate through the joint with respect to various  $K_j$ ,  $K_m$ ,  $b$ , and  $P$ .

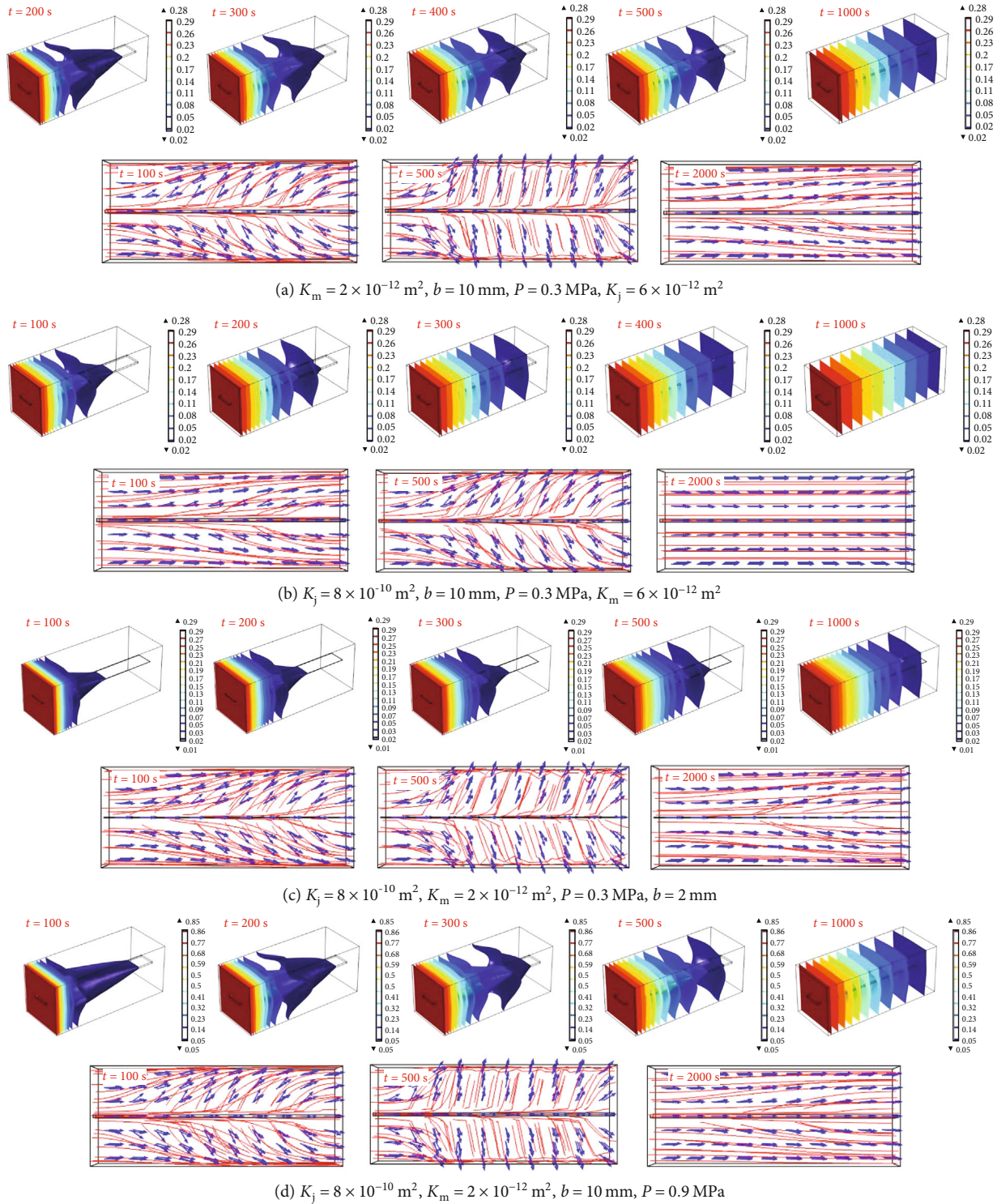


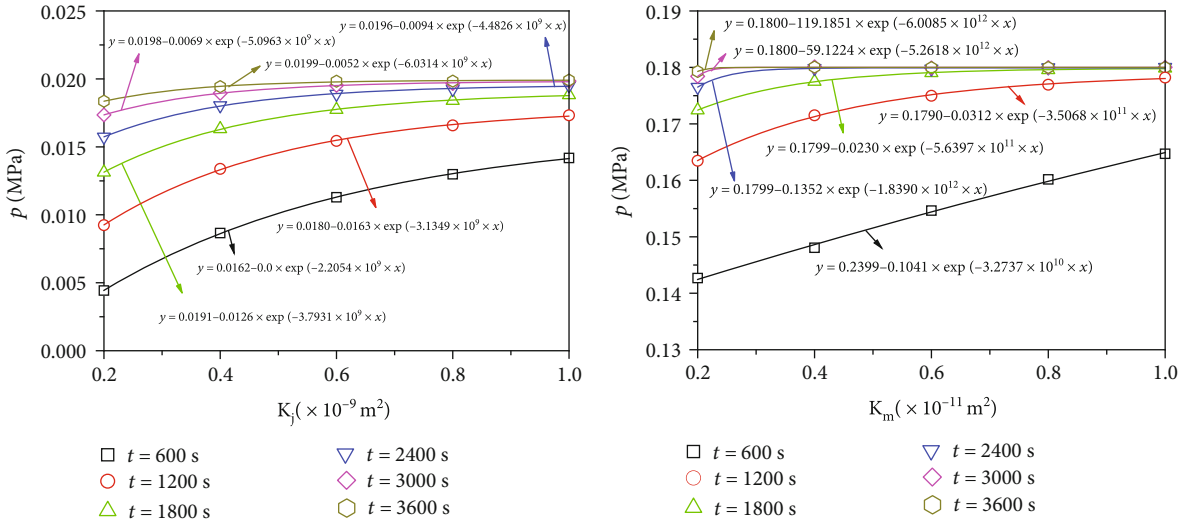
FIGURE 14: Water pressure contour planes and streamlines of flow in the models with various  $K_j$ ,  $K_m$ ,  $b$ , and  $P$ .

transfer to a series of parallel planes perpendicular to the joint direction.

From the evolution characteristics of flow streamlines through the jointed rock mass, at the initial stage, fluid flowing at the left model boundary generally spreads along the

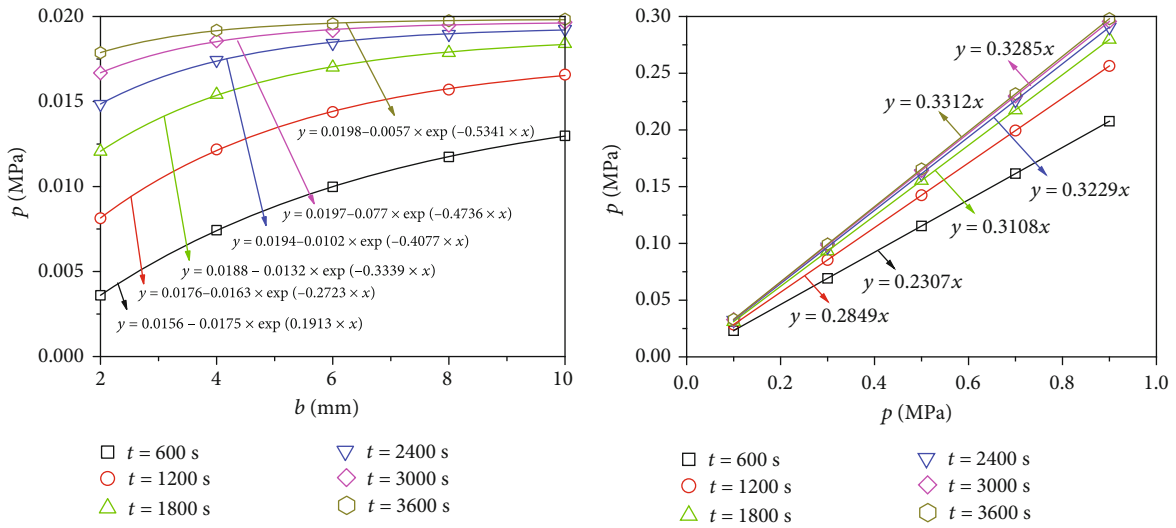
horizontal direction. Later, the flow path changes to the “joint-matrix” direction due to a larger  $K_j$  compared to  $K_m$ . Then, as  $t$  continuously increases, the flow direction transfers to the horizontal direction along the whole model section, and fluid flowing approaches the steady state.





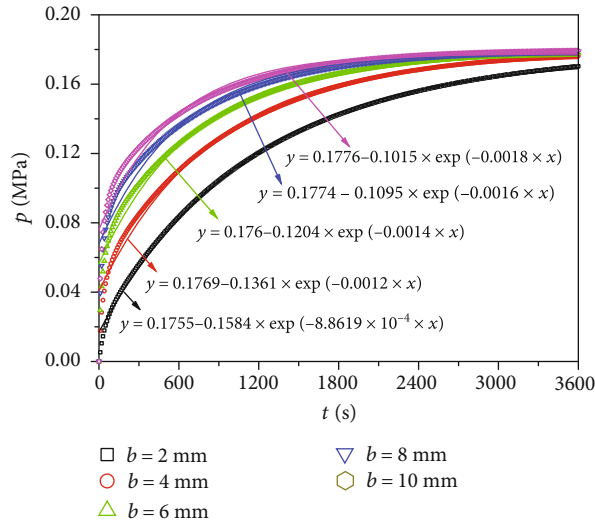
(a)  $p \sim K_j$  ( $L = 0.7$  m,  $t = 600 \sim 3600$  s)

(b)  $p \sim K_m$  ( $L = 0.3$  m,  $t = 600 \sim 3600$  s)



(c)  $p \sim b$  ( $L = 0.7$  m,  $t = 600 \sim 3600$  s)

(d)  $p \sim P$  ( $L = 0.5$  m,  $t = 600 \sim 3600$  s)



(e)  $p \sim t$  ( $L = 0.3$  m,  $b = 2 \sim 10$  mm)

FIGURE 15: Regression analysis of  $p$  as a function of  $K_j$ ,  $K_m$ ,  $b$ ,  $P$ , and  $t$ .

TABLE 3: Regression evaluation of the genetic algorithm for the numerical data.

Index	MSE	RMSE	MAE	MAPE (%)	R	R <sup>2</sup>	Note
Value	$2.60122 \times 10^{-6}$	0.00161	0.00099	0.00024	0.99729	0.99459	$p$
	$5.30998 \times 10^{-5}$	0.00729	0.00382	0.01100	0.99929	0.99859	$v$

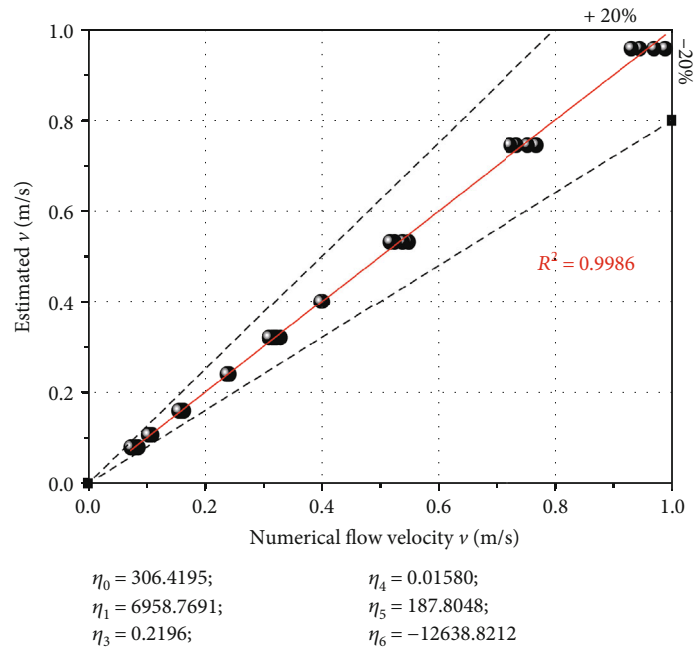
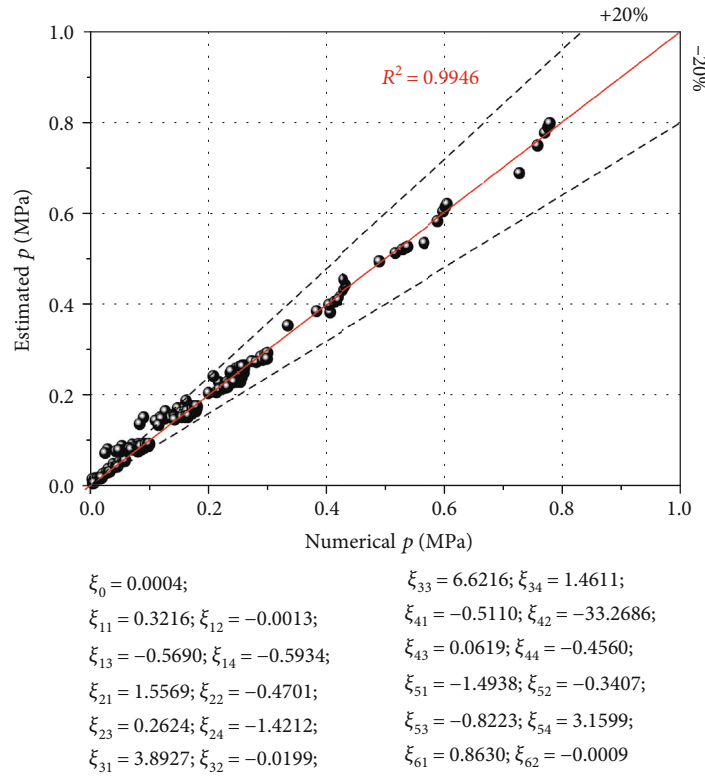


FIGURE 16: Correlation between the calculated values of the genetic algorithm and numerical data.

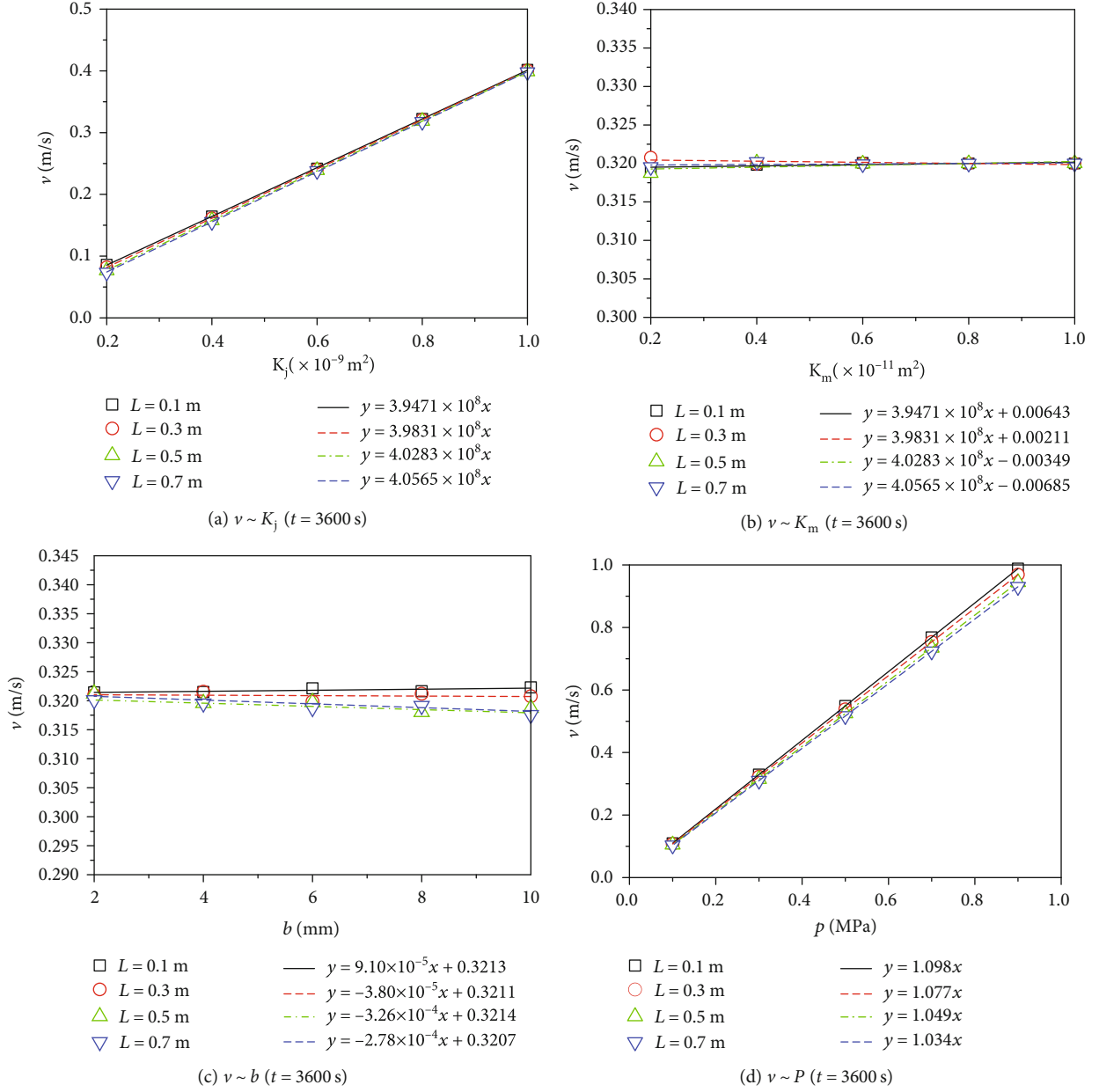


FIGURE 17: Regression analysis of  $v$  as a function of  $K_j$ ,  $K_m$ ,  $b$ ,  $P$ , and  $t$ .

#### 4. Theoretical Prediction Model of the Coupling Effects

From the numerical results discussed above, for a rock mass containing a joint, the evolution process of pore water pressure  $p$  depends on all the factors of  $K_j$ ,  $K_m$ ,  $b$ ,  $P$ ,  $L$ , and  $t$ . Variations in  $p$  as a function of  $L$  can be calculated using equation (2), and variations in  $p$  in terms of  $K_j$ ,  $K_m$ ,  $b$ ,  $P$ , and  $t$  can be described using the following equations, respectively:

$$p = A_1 + B_1 \times \exp(C_1 \times K_j), \quad (3)$$

$$p = A_2 + B_2 \times \exp(C_2 \times K_m), \quad (4)$$

$$p = A_3 + B_3 \times \exp(C_3 \times b), \quad (5)$$

$$p = A_4 + B_4 \times P, \quad (6)$$

$$p = A_5 + B_5 \times \exp(C_5 \times t), \quad (7)$$

where  $A_1, A_2, A_3, A_4, A_5, B_1, B_2, B_3, B_4, B_5, C_1, C_2, C_3$ , and  $C_5$  are fitting coefficients.

Figure 15 presents the regression analysis of  $p$  as a function of  $K_j$ ,  $K_m$ ,  $b$ ,  $P$ , and  $t$ , respectively, using the above equations (3), (4), (5), (6), and (7). Here, for Figures 15(a)–15(d),  $t = 600, 1200, 1800, 2400, 3000$ , and  $3600$  s were, respectively, chosen, and for Figure 15(e), the  $p$  versus  $t$  curves were chosen from numerical results for the jointed rock mass with various  $b$  values. Obviously, the numerical values show a

good agreement with the fitting curves, with all residual squared  $R^2$  values larger than 0.95, indicating that equations (3), (4), (5), (6), and (7) fit the relations of  $p \sim K_j$ ,  $p \sim K_m$ ,  $p \sim b$ ,  $p \sim P$ , and  $p \sim t$  very well.

The polynomial interpolation method can be applied to well evaluate the relations between various influencing factors and the pore water pressure  $p$ . Here, a seven-dimensional space of  $p = f(K_j, K_m, b, P, t, L)$  was established by the coupling effects of six factors. According to the effects of these six factors on  $p$  described in equations (3), (4), (5), (6), and (7), the following equation (6) can be proposed:

$$p = \xi_0 [\xi_{11} \exp(\xi_{12}t + \xi_{13}) + \xi_{14}] [\xi_{21} \exp(\xi_{22}L + \xi_{23}) + \xi_{24}] \cdot [\xi_{31} \exp(\xi_{32}K_j + \xi_{33}) + \xi_{34}] [\xi_{41} \exp(\xi_{42}K_m + \xi_{43}) + \xi_{44}] \cdot [\xi_{51} \exp(\xi_{52}b + \xi_{53}) + \xi_{54}] [\xi_{61}P + \xi_{62}], \quad (8)$$

where  $\xi_0, \xi_{11}, \xi_{12}, \xi_{13}, \xi_{14}, \xi_{21}, \xi_{22}, \xi_{23}, \xi_{24}, \xi_{31}, \xi_{32}, \xi_{33}, \xi_{34}, \xi_{41}, \xi_{42}, \xi_{43}, \xi_{44}, \xi_{51}, \xi_{52}, \xi_{53}, \xi_{54}, \xi_{61},$  and  $\xi_{62}$  are decision parameters.

Equation (8) is a combination of equations (2), (3), (4), (5), (6), and (7), and whether the calculated  $p$  agrees with the numerical results depends on whether the decision parameters are reasonable. Then, a genetic algorithm was constructed to optimize the decision parameters according to the characterization method proposed by Wang and Kong [34] and Wu et al. [24]. This was done through the process of sample series construction, coding, generation of the initial population, calculation of the  $p$  values, solution to fitness, selection operation, crossover operation, mutation operation, and the stop breeding condition setting [35, 36]. The indexes including the mean square error (MSE), root mean square error (RMSE), mean absolute error (MAE), and the mean absolute percentage error (MAPE) were introduced to evaluate the correlation between the optimal calculated results and numerical values, as shown in Table 3. Figure 16(a) displays the correlation between the calculated values obtained from the genetic algorithm and numerical results, with the calculated values of the decision parameters in equation (8). The error between the calculated values and numerical results is quite low, with the correlated coefficient  $R^2$  value of 0.9946, indicating a high reliability of the genetic algorithm.

As discussed in Section 3.2, the dynamic evolution process of the flow velocity  $v$  is also a function of  $K_j$ ,  $K_m$ ,  $b$ , and  $P$  (Figure 17). However, changes in  $v$  versus  $t$  and  $L$  cannot be well characterized using a certain function (Figure 13). For  $t = 3600$  s, variations in  $v$  versus  $K_j$  and  $P$  can be analyzed with a linear function, while  $v$  keeps generally constant with an increase in  $K_m$  and  $b$ . Therefore, a three-dimensional space of  $v = f(K_j, P)$  was built to evaluate the coupling effects of  $K_j$  and  $P$ :

$$v = \eta_0 (\eta_1 K_j + \eta_2) (\eta_3 P + \eta_4) + \eta_5, \quad (9)$$

where  $\eta_0, \eta_1, \eta_2, \eta_3, \eta_4,$  and  $\eta_5$  are decision parameters.

The indexes including MSE, RMSE, MAE, and MAPE are also listed in Table 3, and Figure 16(b) shows the relationships between numerical  $v$  and the calculated  $v$  values using equation (9), with a  $R^2$  value of 0.9986, implying that equation (9) gives a good evaluation of the coupling influences.

## 5. Conclusions

- (1) A conceptual model characterizing the geomechanical states of a water-resistant slab was established, from which, a high-resolution apparatus for seepage tests of a 3D large-scale rock mass and the corresponding experimental method were developed. Then, hydromechanical tests for a large-scale rock mass (300 × 300 × 900 mm) containing a filling joint with the boundary stress of 5 MPa and an inlet water pressure of 0.3 MPa were conducted
- (2) Evolution characteristics of pore water pressures along the joint length with time were experimentally analyzed, which first sharply increases and then gradually approaches constant values and can be well described using an exponential function. At the steady state, the pore water pressure shows a linear decrease of 92.95% along the joint length. Due to migration of fillings, connected flowing channels are produced and water inrush phenomenon happens
- (3) The influences of filling joint permeability, matrix permeability, joint thickness, and inlet water pressure on seepage evolution were numerically evaluated. The stable pore water pressure, which is independent of  $K_j$ ,  $K_m$  or  $b$ , decreases with the joint length but increases with the inlet water pressure. The stable flow velocity presents an increase with  $K_j$  and  $P$ , but exhibits constant values independent of  $K_m$  and  $b$ . The water pressure contour planes gradually transfer from a “funnel shape” to parallel planes perpendicular to the joint direction, and the flow paths change from “joint-matrix” to horizontal direction along the whole model section
- (4) The comprehensive relation was established to describe the coupling influences of  $K_j$ ,  $K_m$ ,  $b$ ,  $P$ ,  $L$ , and  $t$  on the pore water pressure and flow velocity, for which, the decision parameters were, respectively, determined and optimized by the genetic algorithm. The discreteness between the calculated results and numerical values was evaluated. The prediction of the evolution characteristics of pore water pressure and flow velocity was realized

## Data Availability

If needed, we can supply all the data.

## Conflicts of Interest

The authors declare that they have no conflicts of interest.



## Acknowledgments

The authors gratefully acknowledge the financial support from the National Natural Science Foundation of China (51904290, 51734009), the Natural Science Foundation of Jiangsu Province, China (BK20180663), and the Opening Fund of State Key Laboratory of Geohazard Prevention and Geoenvironment Protection (Chengdu University of Technology), China (SKLGP2020K021).

## References

- [1] S. C. Li, C. L. Gao, Z. Q. Zhou et al., "Analysis on the precursor information of water inrush in karst tunnels: a true triaxial model test study," *Rock Mechanics and Rock Engineering*, vol. 52, no. 2, pp. 373–384, 2019.
- [2] Z. Li, H. Liu, Z. Dun, L. Ren, and J. Fang, "Grouting effect on rock fracture using shear and seepage assessment," *Construction and Building Materials*, vol. 242, Article ID 118131, 2020.
- [3] Z. Huang, X. Z. Li, S. J. Li, K. Zhao, and R. Zhang, "Investigation of the hydraulic properties of deep fractured rocks around underground excavations using high-pressure injection tests," *Engineering Geology*, vol. 245, pp. 180–191, 2018.
- [4] Z. Li, H. Zhou, D. Hu, and C. Zhang, "Yield criterion for rock-like geomaterials based on strain energy and CMP model," *International Journal of Geomechanics*, vol. 20, no. 3, Article ID 04020013, 2020.
- [5] Y. C. Wang, H. W. Jing, L. Y. Yu, H. J. Su, and N. Luo, "Set pair analysis for risk assessment of water inrush in karst tunnels," *Bulletin of Engineering Geology and the Environment*, vol. 76, no. 3, pp. 1199–1207, 2017.
- [6] K. Bian, M. Xiao, and J. Chen, "Study on coupled seepage and stress fields in the concrete lining of the underground pipe with high water pressure," *Tunnelling and Underground Space Technology*, vol. 24, no. 3, pp. 287–295, 2009.
- [7] Z. Li, S. Liu, W. Ren, J. Fang, Q. Zhu, and Z. Dun, "Multiscale laboratory study and numerical analysis of water-weakening effect on shale," *Advances in Materials Science and Engineering*, vol. 2020, Article ID 5263431, 2020.
- [8] C. S. Wang, Y. J. Jiang, H. J. Luan, and S. Sugimoto, "Effect of shearing on hydraulic properties of rough-walled fractures under different boundary conditions," *Energy Science & Engineering*, vol. 8, no. 3, pp. 865–879, 2020.
- [9] H. M. Jiang, L. Li, X. L. Rong, M. Y. Wang, Y. P. Xia, and Z. C. Zhang, "Model test to investigate waterproof-resistant slab minimum safety thickness for water inrush geohazards," *Tunnelling and Underground Space Technology*, vol. 62, pp. 35–42, 2017.
- [10] R. C. Liu, B. Li, and Y. J. Jiang, "Critical hydraulic gradient for nonlinear flow through rock fracture networks: the roles of aperture, surface roughness, and number of intersections," *Advances in Water Resources*, vol. 88, pp. 53–65, 2016.
- [11] K. B. Min, J. Rutqvist, C. F. Tsang, and L. Jing, "Stress-dependent permeability of fractured rock masses: a numerical study," *International Journal of Rock Mechanics and Mining Sciences*, vol. 41, no. 7, pp. 1191–1210, 2004.
- [12] C. Tian, Y. Liu, X. Yang, Q. Hu, B. Wang, and H. Yang, "Development characteristics and field detection of overburden fracture zone in multiseam mining: a case study," *Energy Science & Engineering*, vol. 8, no. 3, pp. 602–615, 2020.
- [13] Q. Wang, H. Gao, H. C. Yu, B. Jiang, and B. Liu, "Method for measuring rock mass characteristics and evaluating the grouting-reinforced effect based on digital drilling," *Rock Mechanics and Rock Engineering*, vol. 52, no. 3, pp. 841–851, 2019.
- [14] Q. Yin, H. W. Jing, R. C. Liu, G. W. Ma, L. Y. Yu, and H. J. Su, "Experimental study on stress-dependent nonlinear flow behavior and normalized transmissivity of real rock fracture networks," *Geofluids*, vol. 2018, Article ID 8217921, 16 pages, 2018.
- [15] Q. Yin, H. W. Jing, H. J. Su, and H. H. Zhao, "Experimental study on mechanical properties and anchorage performances of rock mass in the fault fracture zone," *International Journal of Geomechanics*, vol. 18, no. 7, article 04018067, 2018.
- [16] Z. Jiang, Q. Li, Q. Hu et al., "Underground microseismic monitoring of a hydraulic fracturing operation for CBM reservoirs in a coal mine," *Energy Science & Engineering*, vol. 7, no. 3, pp. 986–999, 2019.
- [17] D.-x. Liang, Z.-q. Jiang, S.-y. Zhu, Q. Sun, and Z.-w. Qian, "Experimental research on water inrush in tunnel construction," *Natural Hazards*, vol. 81, no. 1, pp. 467–480, 2016.
- [18] D. Pan, S. Li, Z. Xu, P. Lin, and X. Huang, "Experimental and numerical study of the water inrush mechanisms of underground tunnels due to the proximity of a water-filled karst cavern," *Bulletin of Engineering Geology and the Environment*, vol. 78, no. 8, pp. 6207–6219, 2019.
- [19] Y. Zhao, P. F. Li, and S. M. Tian, "Prevention and treatment technologies of railway tunnel water inrush and mud gushing in China," *Journal of Rock Mechanics and Geotechnical Engineering*, vol. 5, no. 6, pp. 468–477, 2013.
- [20] T. X. Hou, X. G. Yang, H. G. Xing, K. X. Huang, and J. W. Zhou, "Forecasting and prevention of water inrush during the excavation process of a diversion tunnel at the Jinping II Hydropower Station, China," *Springerplus*, vol. 5, no. 1, p. 700, 2016.
- [21] D. Ma, X.-x. Miao, Y. Wu et al., "Seepage properties of crushed coal particles," *Journal of Petroleum Science and Engineering*, vol. 146, pp. 297–307, 2016.
- [22] L. Q. Shi and R. N. Singh, "Study of mine water inrush from floor strata through faults," *Mine Water and the Environment*, vol. 20, no. 3, pp. 140–147, 2001.
- [23] X. T. Wang, S. C. Li, Z. H. Xu, J. Hu, D. Pan, and Y. Xue, "Risk assessment of water inrush in karst tunnels excavation based on normal cloud model," *Bulletin of Engineering Geology and the Environment*, vol. 78, no. 5, pp. 3783–3798, 2019.
- [24] J. Y. Wu, G. S. Han, M. M. Feng et al., "Mass-loss effects on the flow behavior in broken argillaceous red sandstone with different particle-size distributions," *Comptes Rendus Mecanique*, vol. 347, no. 6, pp. 504–523, 2019.
- [25] J. Zhao, L. Yin, and W. Guo, "Stress-seepage coupling of cataclastic rock masses based on digital image technologies," *Rock Mechanics and Rock Engineering*, vol. 51, no. 8, pp. 2355–2372, 2018.
- [26] Z. Huang, W. Zeng, Y. Wu, S. Li, and K. Zhao, "Experimental investigation of fracture propagation and inrush characteristics in tunnel construction," *Natural Hazards*, vol. 97, no. 1, pp. 193–210, 2019.
- [27] P. S. Lang, A. Paluszny, and R. W. Zimmerman, "Permeability tensor of three-dimensional fractured porous rock and a comparison to trace map predictions," *Journal of Geophysical Research: Solid Earth*, vol. 119, no. 8, pp. 6288–6307, 2014.

- [28] I. Vazaios, N. Vlachopoulos, and M. S. Diederichs, "Assessing fracturing mechanisms and evolution of excavation damaged zone of tunnels in interlocked rock masses at high stresses using a finite-discrete element approach," *Journal of Rock Mechanics and Geotechnical Engineering*, vol. 11, no. 4, pp. 701–722, 2019.
- [29] C. Deng and D. M. Martinez, "Viscous flow in a channel partially filled with a porous medium and with wall suction," *Chemical Engineering Science*, vol. 60, no. 2, pp. 329–336, 2005.
- [30] F. Ye, J.-C. Duan, W.-X. Fu, and X.-Y. Yuan, "Permeability properties of jointed rock with periodic partially filled fractures," *Geofluids*, vol. 2019, Article ID 4039024, 14 pages, 2019.
- [31] Q. Yin, H. W. Jing, H. J. Su, and H. D. Wang, "CO<sub>2</sub> permeability analysis of caprock containing a single fracture subject to coupled thermal-hydromechanical effects," *Mathematical Problems in Engineering*, vol. 2017, Article ID 1290748, 13 pages, 2017.
- [32] L. Zou, L. Jing, and V. Cvetkovic, "Roughness decomposition and nonlinear fluid flow in a single rock fracture," *International Journal of Rock Mechanics and Mining Sciences*, vol. 75, pp. 102–118, 2015.
- [33] L. Zou, L. Jing, and V. Cvetkovic, "Shear-enhanced nonlinear flow in rough-walled rock fractures," *International Journal of Rock Mechanics and Mining Sciences*, vol. 97, pp. 33–45, 2017.
- [34] L. Z. Wang and H. L. Kong, "Variation characteristics of mass-loss rate in dynamic seepage system of the broken rocks," *Geofluids*, vol. 2018, Article ID 7137601, 17 pages, 2018.
- [35] J. R. Ruiseco, J. Williams, and M. Kumral, "Optimizing ore-waste dig-limits as part of operational mine planning through genetic algorithms," *Natural Resources Research*, vol. 25, no. 4, pp. 473–485, 2016.
- [36] M. E. Villalba Matamoros and M. Kumral, "Correction to: calibration of genetic algorithm parameters for mining-related optimization problems," *Natural Resources Research*, vol. 28, no. 2, pp. 457–459, 2019.